

The formation and evolution of planetary systems: Grain growth and chemical processing of dust in T Tauri systems.

J. Bouwman and Th. Henning

Max Planck Institute for Astronomy, Königstuhl 17, D-69117, Heidelberg, Germany
and

L. A. Hillenbrand

Department of Astronomy, California Institute of Technology, Pasadena, CA 91125.
and

M.R. Meyer and I. Pascucci

Steward Observatory, University of Arizona, 933 N. Cherry Ave., Tucson, AZ 85721-0065
and

J. Carpenter

Department of Astronomy, California Institute of Technology, Pasadena, CA 91125.
and

D. Hines

Space Science Institute, 4750 Walnut Street, Suite 205 Boulder, CO 80301.
and

J.S. Kim and M.D. Silverstone

Steward Observatory, University of Arizona, 933 N. Cherry Ave., Tucson, AZ 85721-0065
and

D. Hollenbach

NASA Ames Research Center, Moffet Field, CA 94035

and

S. Wolf

Max Planck Institute for Astronomy, Königstuhl 17, D-69117, Heidelberg, Germany

ABSTRACT

This paper is one in a series presenting results obtained within the Formation and Evolution of Planetary Systems (FEPS) Legacy Science Program on the *Spitzer Space Telescope*. Here we present a study of dust processing and growth in seven protoplanetary disks. Our spectra indicate that the circumstellar silicate dust grains have grown to sizes at least 10 times larger than observed in the interstellar medium, and show evidence for a non-negligible ($\sim 5\%$ in mass fractions) contribution from crystalline species. These results are similar to those of other studies of protoplanetary disks. In addition, we find a correlation between the strength of the amorphous silicate feature and the shape of the spectral energy distribution. This latter result is consistent with the growth and subsequent gravitational settling of dust grains towards the disk mid-plane. Further, we find a change in the relative abundance of the different crystalline species: more enstatite relative to forsterite is observed in the inner warm dust population at ~ 1 AU, while forsterite dominates in the colder outer regions at ~ 5 to 15 AU. This change in the relative abundances argues for a localized crystallization process rather than a radial mixing scenario where crystalline silicates are being transported outwards from a single formation region in the hot inner parts of the disk. Last, we report the detection of emission from polycyclic aromatic hydrocarbon molecules in five out of seven sources. We find a tentative PAH band at $8.2 \mu\text{m}$, previously undetected in the spectra of disks around low-mass pre-main-sequence stars.

Subject headings: pre-main-sequence stars – circumstellar disks — circumstellar dust — planetary systems

1. Introduction

The circumstellar disks surrounding the pre-main-sequence Brown Dwarfs (BD), T Tauri stars (TTS) and Herbig Ae/Be

(HAEBE) systems are believed to be the sites of ongoing planet formation (e.g. Luhman et al. 2007; Natta et al. 2007, from here on we will refer to these disks

as protoplanetary disks). As most of the youngest (<1 Myr) solar-mass stars have circumstellar disks (Strom et al. 1989), with typical masses (Beckwith et al. 1990) and sizes (McCaughrean & O'Dell 1996; Dutrey et al. 1996) comparable to the expected values for the primitive solar nebula, these disks are the natural candidates for the birth-sites of planets. The sub-micron sized dust grains present initially in these disks can coagulate to form larger objects and eventually earth-like planets (e.g. Weidenschilling 1997; Henning et al. 2006). By deriving the composition of the circumstellar dust, and identifying the processes governing the chemistry and coagulation, valuable insights can be gained in the workings of protoplanetary disks (e.g. Bouwman et al. 2001, 2003; van Boekel et al. 2003, 2005; Przygodda et al. 2003; Kessler-Silacci et al. 2006a; Sargent et al. 2006) and thus the planet formation process. The results of these analyses can be compared directly with the investigation of solar system objects like comets, meteorites and interplanetary dust particles (IDPs), which preserve a record of the early phases in the evolution of the solar system.

With the IRAS and ISO missions, a tremendous advance in our knowledge of protoplanetary disks was achieved. However, the spectroscopic studies with these missions were limited to relatively nearby and luminous stars of spectral type A and B, and provided only limited knowledge of the evolution of solar-mass systems. With the launch of the *Spitzer Space Telescope* (Werner et al. 2004), these less luminous systems became accessible to observations. The FEPS *Spitzer* Legacy program probes

the circumstellar dust properties around a representative sample of protoplanetary disks and debris disks, spanning a wide range of circumstellar disk properties and covering the major phases of planet system formation and evolution (Meyer et al. 2006)

We present an analysis of the infrared (IR) spectra of protoplanetary disks around seven pre-main sequence systems observed within the FEPS legacy program. These are the only systems among the 328 FEPS targets showing spectroscopic features from solid state dust components. (See Meyer et al. 2006, for a detailed description of the FEPS parent sample). In Table 1 the astrophysical parameters of these seven stars are compiled. Five of the systems, RX J1842.9-3532, RX J1852.3-3700, 1RXS J132207.2-693812, RX J1111.7-7620, and 1RXS J161410.6-230542, were identified in Silverstone et al. (2006) as optically-thick primordial disks on the basis of their IRAC colors and excess emission at wavelengths shorter than 8 μm . Silverstone et al. (2006) provide a literature review for the five stars identified in their study. In addition to these five systems, HD 143006 and RX J1612.6-1859A also show evidence for optically-thick disks and solid state features. We give a literature review for the latter two stars in Appendix A. HD 143006 was added to the FEPS sample on the basis of its IRAS excess emission, in order to search for remnant gas in that system (e.g. Pascucci et al. 2006). The solid state features in RX J1612.6-1859A were noticed from visual inspection of its spectrum. No other sources in the FEPS sample show evidence for solid state emission features.

Of these 321 sources, most lack excess in the IRS wavelengths, and a few exhibit optically-thin emission from debris. No other optically-thick circumstellar disk sources are present in the data other than the seven with solid state emission features discussed here.

We study the compositional properties of the systems listed in Table 1 using 5–35 μm spectra obtained with the Infrared Spectrograph (IRS; Houck et al. 2004) on-board the *Spitzer Space Telescope*. We focus on silicate grain processing (silicates make up the bulk of the refractory dust mass assuming solar system abundances) and perform a quantitative analysis of the observed solid state emission. Using a consistent analysis method for the entire sample, the derived grain composition of the individual systems can be compared directly. This enables us look for signs of silicate grain processing. Apart from analyzing the 10 μm spectral region, also accessible to ground-based studies, *Spitzer* provides access to the silicate resonances at longer wavelengths. This enables us to study the dust composition of not only the warmest dust (temperatures between $\sim 500 - 1000$ K), located in the inner parts ($\sim 0.1 - 1$ AU) of the protoplanetary disks around solar-like stars, but also the cold (~ 100 K) dust component in the outer regions (~ 15 AU) of the disks.

This paper is organized in the following way: In section 2 we discuss the data reduction, introduce the main dust components and present the method used to analyze the Spitzer IRS spectra. In section 3 modelling results are presented and in section 4 we discuss implications for the evolution of the dust in the circumstellar

disks around solar-mass stars.

2. Observations and Dust Models

2.1. The IRS Low-Resolution Spectra

We obtained low-resolution ($R = \sim 60 - 120$) spectra with the IRS instrument on-board *Spitzer*. A high accuracy IRS or PCRS peak-up (with a 1σ pointing uncertainty of $0.4''$ radius) was used to acquire targets in the spectrograph slit, thus minimizing slit losses and assuring high photometric accuracy to about 10%. Two nod positions per cycle were obtained in standard staring mode with a minimum of six cycles per target for redundancy and to allow the rejection of artifacts introduced by bad pixels or cosmic ray hits. The integration times were 6s and 14s for the brightest and faintest sources, respectively. The targets were observed with the full spectral coverage of the IRS low-resolution instrument between 5.2 and 35 μm . Beyond 35 μm the spectra suffer from excess noise (Houck et al. 2004) and can not be used.

Our spectra are based on the **droopres** intermediate data product processed through the SSC pipeline S12.0.2. Partially based on the **SMART** software package (Higdon et al. 2004, for details on this tool and extraction methods), our data is further processed using spectral extraction tools developed for the FEPS *Spitzer* science legacy program. As a first step, we correct for the background emission and stray-light by subtracting the associated pairs of imaged spectra of the two nodded positions along the slit for each module and order. In this way we also correct for pixels having an anomalous dark current. Pixels flagged

by the SSC data pipeline as “bad” were replaced with a value interpolated from an 8 pixel perimeter surrounding the errant pixel. We then extracted the spectra from the resulting set of images using a 6.0 pixel and 5.0 pixel fixed-width aperture in the spatial dimension for the observations with the short- (5.2 - 14 μm) and long-wavelength (14-35 μm) modules, respectively. The low-level fringing at wavelengths >20 μm was removed using the `irsfringe` package (Lahuis & Boogert 2003).

Absolute flux calibration was achieved in a self-consistent manner using the ensemble of FEPS observations. As the majority of the 328 FEPS program stars exhibit stellar photospheres throughout the shorter wavelength range of the IRS, this data set is unique for calibrating the IRS instrument. From our full set of FEPS observations we selected a subset of the spectra which complied with the following criteria: 1) colors (24-33 μm) within 1σ of an extrapolated best-fit model photosphere (e.g. Meyer et al. 2004; Carpenter et al. 2006) and 2) Signal-to-noise ratio (SNR) larger than 50 with no artifacts within the spectra. This resulted for the first order of the short wavelength module (SL1) and the long wavelength module spectra (LL1, LL2) in a set of 16 stars and for the shorter wavelength orders (SL2) in a subset of 10 stars. Together with the stellar photospheric models for these two subsets, we used these spectra to derive the relative spectral response functions (RSRFs) for the absolute flux calibration. For the relative (point to point) calibration, we derived RSRFs using six calibration stars observed at different epochs with the Co-

hen photospheric models provided by the SSC, having a superior SNR. This procedure ensures that the RSRFs used to calibrate our protoplanetary disk spectra have the highest possible SNR and an estimated absolute flux calibration uncertainty of $\sim 10\%$. For further details on the flux calibration see the explanatory supplement for the FEPS data, delivered to the *Spitzer* data archive (Hines et al. 2005).

The resulting calibrated spectral energy distributions are shown in Fig. 1. A detailed view of these spectra in three wavelength bands, showing more clearly the solid-state emission features is presented in Fig. 2. As one can see from Fig. 1, a wide range in spectral shape and emission feature strength can be observed. In the next section we will discuss the analysis methods and the different silicate components and grain models used to interpret the spectra shown in Fig. 2.

2.2. Outline of Spectral Analysis Methods

For the analysis and interpretation of our observations we use a two-fold approach. First, we characterize the spectra by measuring the strengths and positions of spectral features. Second, we decompose the observed emission features to determine the relative contribution of different silicate grains. For the spectral characterization we employ a method similar to schemes previously used to analyze IR spectra from the Infrared Space Observatory (e.g. Molster et al. 2002a,b) and ground-based observations (e.g. van Boekel et al. 2005). To measure the emission band strengths and positions, we first fit a low order polynomial (second order in the 10 μ

region, fifth order for $\lambda > 15 \mu\text{m}$) to the spectral data points excluding obvious spectral features (e.g. the continuum). As a next step we normalize our spectra to the fitted continuum as $F_{\nu,\text{norm}} = 1 + (F_{\nu,\text{obs}} - F_{\nu,\text{cont}}) / \langle F_{\nu,\text{cont}} \rangle$, where $F_{\nu,\text{obs}}$ is the observed Spitzer flux, $F_{\nu,\text{cont}}$ is the fitted continuum, and $\langle F_{\nu,\text{cont}} \rangle$ the mean continuum value over the fitted wavelength interval. This normalization allows us to directly compare the different spectra and, ensures that the shape of the spectral features remains identical to that in the original, unnormalized, spectra.

To characterize the $10 \mu\text{m}$ amorphous silicate band we determined the fluxes at different wavelengths across the silicate feature in the normalized spectra. The results of this analysis are presented in Section 3. Amorphous silicates also show a band at around $18 \mu\text{m}$. However, this band blends with the (often rising) continuum emission, as can for instance be seen in Fig. 1. This makes it difficult, if not impossible, to determine the band strength and position with sufficient accuracy for a meaningful analysis. We, therefore, opted not to use this band in our analysis. At longer ($>20 \mu\text{m}$) wavelengths the emission features are mainly produced by crystalline silicates. To measure the observed band positions and strengths, we simultaneously fitted a Gaussian to each of the main spectral features in the normalized spectra. The results of this analysis are also presented in Section 3. For the crystalline silicate emission bands in the $10 \mu\text{m}$ wavelength region, a slightly modified analysis method has to be applied. In this wavelength range, the emission bands overlap with, and can be dominated by emis-

sion from small amorphous silicate grains. Also, PAH molecules may contribute to the observed emission in the short wavelength range, overlapping with the emission features of the crystalline silicates. Therefore, the crystalline contribution can only be estimated by fitting a detailed grain model (discussed in the next section) determining the contribution of the amorphous silicates and PAH molecules. After subtracting the fitted contribution of the amorphous silicate and PAH molecules, we applied an analysis for estimating the different crystalline silicate band strengths in the $10 \mu\text{m}$ wavelength region, similar to that for the longer wavelength crystalline bands.

2.3. Dust Models

The grain model and analysis method for determining the physical properties of the dust grains contributing to the observed emission are similar to those successfully applied in previous studies of the $10 \mu\text{m}$ region (see Bouwman et al. 2001; van Boekel et al. 2005, for further discussion). Here, we also apply this method to the silicate emission at longer ($\sim 20\text{-}30 \mu\text{m}$) wavelengths. Dust in protoplanetary disks has most likely the structure of highly irregular aggregates containing many different dust constituents, like the interplanetary dust particles collected in the Earth's upper atmosphere. Calculating the optical properties of such complex structure has proven to be extremely difficult (e.g. Henning & Stognienko 1996). However, assuming that the aggregates are extremely porous, the individual constituents making up the aggregate may interact with the radiation field as separate entities, as is the case of IDPs (Molster et al.

2003). Therefore, we assume that the observed emission can be represented by the sum of the emission of individual dust species. Table 2 summarizes the dust species used in our analysis, including all dust species commonly identified in protoplanetary disks (e.g. Bouwman et al. 2001; van Boekel et al. 2005; Sargent et al. 2006).

Crystalline silicates such as forsterite (Mg_2SiO_4) and enstatite (MgSiO_3) have many strong and narrow resonances in the wavelength range covered by the IRS spectrograph. These rotational/vibrational bands of the crystalline dust species allow for a much more accurate determination of the chemical composition, grain size and shape/porosity compared to the amorphous silicates. We find, like in the above mentioned studies, that the pure magnesium end-members of the olivine and pyroxene families give the best match to the observed spectral features. Based on the comparison between the in our spectra observed band positions and strengths, and laboratory measurements (Fabian et al. 2001; Koike et al. 2003), we find no evidence for iron containing crystalline silicates. Still a few open questions remain. Enstatite comes in the form of clino- and ortho-enstatite, both having a different crystalline structure. However, both forms show very similar emission bands at around $10 \mu\text{m}$, making it hard to distinguish between them (e.g. Jäger et al. 1998; Koike et al. 2000). Only at the longer wavelengths a clear difference between the emission properties can be observed. Unfortunately, as we will discuss in the next chapter, no clear enstatite bands can be observed at the longer wavelengths, mak-

ing it difficult to determine the exact enstatite structure. We, therefore, have chosen to use clino-enstatite, allowing for a direct comparison between our results and the study by van Boekel et al. (2005) of a sample of Herbig Ae/Be stars. A similar problem occurs for silica dust grains. Silica has nine polymorphs among which are quartz, tridimite and cristobalite, differing in crystal structure. While of these silicates quartz is the most common form found on Earth, the common form found in interplanetary dust particles (IDPs) is tridimite (Rietmeijer 1988) and most likely also the most common form in protoplanetary disks. To our knowledge, no similar quality laboratory measurements of tridimite exists, enabling us to perform an identical analysis as for the other dust species. However, if one compares the amorphous form of silica and quartz, we observe similar bands. It might well be, that like in the case of enstatite, it will be difficult to tell the different forms of silica apart. As quartz is unlikely to exist in protoplanetary disks we have opted to use an amorphous silicate with the stoichiometry of silica.

As already was noted in previous studies (e.g. Bouwman et al. 2001), the observed emission bands of forsterite, enstatite and silica can not be reproduced assuming simple homogeneous spherical grains, but that one has to adopt an inhomogeneous grain structure and/or nonspherical grain shape. Here we use a distribution of hollow spheres (DHS; Min et al. 2005) which gives an excellent match to the observed band positions and shapes. DHS has the advantage over the widely used continuous distribution of ellipsoids

(CDE; Bohren & Huffman 1983) that it is also defined outside of the Rayleigh limit, making it possible to investigate the effects of grain size on the emission properties of the grains. One should realize that the above discussed grain models such as DHS or CDE should not be taken as an exact representation of the structure/shape of a grain, but rather as a statistical description of the grain shape and structure and its deviation from sphericity and homogeneity; (see Voshchinnikov et al. 2006; Min et al. 2006, for a further discussion of grain shape and porosity effects).

For the amorphous iron/magnesium silicates the exact composition and grain shape can not be constrained as well as for the crystalline silicates. Models of the broad amorphous silicate resonances at $\sim 10 \mu\text{m}$ and $\sim 18 \mu\text{m}$ are to some extent degenerate. Silicate models with varying magnesium to iron ratios and different grain shapes/homogeneity can reproduce the observed bands (e.g. Min et al. 2007). To allow for a direct comparison with previous studies, we assume here that the amorphous silicates have an equal magnesium to iron atomic ratio, and stoichiometries consistent with olivine and pyroxene. Further, for the amorphous iron-magnesium silicates we assume homogeneous, spherical grains for which we calculate the absorption coefficients using the Mie theory (e.g. Bohren & Huffman 1983) and the optical constants listed in Table 2.

To take into account the effect of grain size, we calculated for each of the different grain species the opacities for three volume equivalent grain radii of $0.1 \mu\text{m}$, $1.5 \mu\text{m}$ and $6.0 \mu\text{m}$, respectively. These grain sizes sample the range of spectroscopically iden-

tifiable grain sizes at infrared wavelengths at the SNR of our data. The resulting calculated opacities for three successive wavelength regimes are shown in Figs. 3a, 3a and 3b. We present our analysis of the various dust species in Sections 3.1, 3.2, and 3.3.

Apart from the silicate dust species, PAH molecules also contribute to the observed emission bands within the spectral range of the IRS instrument. These large molecules are not in thermal equilibrium with the radiation field, but are stochastically heated. Though many of the observed spectral features can be linked to specific vibrational modes and ionization states of the molecules, the exact composition remains unclear. As our main focus in this paper is the solid-state component in the protoplanetary disks, we opted to use a template spectrum, based on observed profiles by Peeters et al. (2002) and van Diedenhoven et al. (2004), for estimating the contribution of PAH molecules to the spectra. We present this analysis in Section 3.4.

The thermal infrared emission from protoplanetary disks is determined by the complex spatial distribution of individual dust species, and the radial and vertical optical depth and temperature distributions. A completely self-consistent model of protoplanetary disks, such as a full radiative transfer calculation, would also have to account for processes such as radial and vertical mixing of circumstellar material and chemical and structural alteration of the dust grains under varying physical conditions in different parts of the disk. Further, to uniquely constrain such models, spatially

resolved observations as a function of wavelength (e.g. Thamm et al. 1994) are necessary. Instead, we employ a more simplistic approach which has been demonstrated to successfully reproduce the silicate emission features of HAEBE and TTS systems. Detailed self-consistent models (e.g. Men'shchikov & Henning 1997; Chiang & Goldreich 1997; Dullemond et al. 2001) have shown that the emission features originate from a warm optically thin disk surface layer on top an optically thick disk interior, producing continuum emission. The basic assumption of our simple model is that the disk emission features can be reproduced by a sum of emissivities at a given temperature T_{dust} , and the continuum emission by the emission of a black body at a given temperature T_{cont} , which could be interpreted as the typical color temperature of the underlying continuum at a given wavelength.

We thus fit the following emission model using a linear least square minimization to the Spitzer low-resolution spectra:

$$\begin{aligned}
 F_\nu &= B_\nu(T_{\text{cont}})C_0 \\
 &+ B_\nu(T_{\text{dust}}) \left(\sum_{i=1}^3 \sum_{j=1}^5 C_{i,j} \kappa_\nu^{i,j} \right) \\
 &+ C_{\text{PAH}} I_\nu^{\text{PAH}}, \quad (1)
 \end{aligned}$$

where $B_\nu(T_{\text{cont}})$ denotes the Planck function at the characteristic continuum temperature T_{cont} , $B_\nu(T_{\text{dust}})$ the Planck function at the characteristic silicate grain temperature T_{dust} , $\kappa_\nu^{i,j}$ is the mass absorption coefficient for silicate species j (five in total) and grain size i (three in total), I_ν^{PAH} is the PAH template emission spectrum, and C_0 , $C_{i,j}$ and C_{PAH} are the weighting factors of the continuum, the silicate com-

ponents and the PAH contribution, respectively. For the single temperature approximation to be meaningful, the width of the spectral region, and thus the temperature range, needs to be sufficiently narrow. Therefore, we have split the observed spectra into three bands: from 6 to 13 μm , from 17 to 26 μm , and from 26 to 36 μm . Apart from the previous considerations, these wavelength boundaries also ensure that both continuum and spectral features can be well characterized, and that multiple bands of the main crystalline silicates can be modeled simultaneously. This latter point is important as it reduces the degeneracy problem of overlapping emission bands of the different dust species. We have limited the maximum temperature in our fits to 1500 K, above which all silicate dust is expected to be vaporized.

Fig. 2 shows the resulting best-fit models for the three spectral regions. As one can see, a good agreement between model and observations can be obtained using the dust species discussed in this section, without the need for additional components. The resulting model parameters are listed in Table 3. We estimate the uncertainties in the derived band strengths and positions and the best-fit dust compositions by a monte-carlo method as discussed in Section 15.6 of (Press et al. 1992): We generate a set of 100 spectra for each observation by randomly adding Gaussian noise with a 1σ distribution equal to the error in the spectral extraction determined for each spectral data point. For each of these simulated spectra, we applied the analysis methods described above. Our quoted results represent the mean values of the derived quantities and the error is the 1σ

standard deviation in the mean.

3. Results

Following the dust modelling and spectral decomposition, our main science results are in the areas of dust coagulation from the analysis of the 10 μm amorphous silicate feature, dust settling from the additional analysis of the overall SED shape, crystallinity from the analysis of the various silicate dust species, and PAHs, which remain in the residual emission after subtracting the identified silicates.

3.1. Coagulation in protoplanetary disks

Grain size strongly influences the infrared opacities, as can be seen in Fig. 3a to 3c. Typically, for the observations presented here, grain sizes (assuming compact grains) of up to 10 μm can be inferred spectroscopically. This is two orders of magnitude larger than the grain sizes typically derived for dust grains in the ISM ($\leq 0.1 \mu\text{m}$). For larger grains, the spectral signatures become too weak to distinguish them from continuum emission. Amorphous iron-magnesium silicates, making up the bulk of the solid state material in the ISM, show two broad spectral features at about 10 μm and 18 μm from which grain sizes can in principle be determined. The latter band, however, often blends with continuum emission from the disk interior and colder dust grains at larger radii, making it difficult to determine the grain size. For this reason, the 10 μm silicate band gives the most accurate information concerning amorphous silicate grain sizes. Many previous studies have shown that both the shape (Bouwman et al. 2001)

and strength (van Boekel et al. 2003, 2005; Przygodda et al. 2003; Schegerer et al. 2006; Kessler-Silacci et al. 2005, 2006a) of the 10 μm silicate features observed in HAEBE and TTS systems are mainly determined by the size of the amorphous silicate grains.

Fig. 4 shows the correlation between the shape and strength of the 10 μm silicate feature as measured by the relation between the peak over continuum strength of the 10 μm silicate feature and the ratio of normalized fluxes at 11.3 to 9.8 μm (filled symbols) and at 8.6 to 9.8 μm (open symbols). We performed a Kendall's τ test on the data plotted in Fig. 4. This test computes the probability that (x,y) pairs of data are correlated in the sense of the relative rank ordering of the x-values compared to the relative rank ordering of the y-values (Press et al. 1992). A value of Kendall's τ was computed along with the two-sided probability that the variables are not correlated ($\tau = -1$ indicates a perfect anti-correlation while $\tau = 1$ indicates a perfect positive correlation). For the solid points in Fig. 4, Kendall's $\tau = -0.905$ with a probability $P < 0.004$ that the data are uncorrelated. For the open points in Fig. 4, we find that $\tau = -0.810$ with a probability $P < 0.011$ that the data are uncorrelated. We interpret these trends as confirmation that the strengths and shapes of the silicate features are correlated. Though crystalline silicate emission bands will also influence the shape of the 10 μm silicate band, the correlations of Fig. 4 can be best explained by a change in the typical size of the emitting dust grains. The dashed line shows the expected correlation for an amorphous silicate of olivine stoichiometry with a grain size changing continuously

from $0.1 \mu\text{m}$ (lower right) to $2 \mu\text{m}$ (upper left). The only exception is the 8.6 over $9.8 \mu\text{m}$ ratio of RX J1612.6-1859A (#3), where the ratio is dominated by an unusually strong emission from enstatite and silica.

Fig. 5 shows the relation between the mass weighed grain size of the amorphous iron-magnesium silicates (open symbols; right axis) as derived from our spectral decomposition of 0.1 , 1.5 and $6 \mu\text{m}$ grains and the peak over continuum value of the $10 \mu\text{m}$ silicate band. Examining this relation in more detail, we find a Kendall's τ of -0.81 for the rank ordering of peak-to-continuum emission compared to the mean size of amorphous silicate grains based on the analysis presented in Table 3. The probability of these variables not being correlated is 0.011 . This correlation demonstrates that the peak to continuum ratio is correlated to the estimated size of the emitting amorphous iron-magnesium silicate grains. As a note of caution, recall that the exact values for the grain sizes derived are linked to the grain model used in the spectral decomposition. For reasons discussed in Section 2.3, we use homogeneous spheres to model the amorphous silicates. More complex grain structures, like fractal high-porosity grains give qualitatively similar results (e.g. Voshchinnikov et al. 2006; Min et al. 2006), but require much larger aggregates to reproduce the observed band strengths.

3.2. Coagulation and dust settling

Having explored grain growth for our sample of T Tauri disks compared to the ISM grain population, we now ask what effect coagulation could have on the disk

structure itself. As we do not have spatially resolved observations, we use the shape of the SED to infer the geometry of the disks. It is long known that the disk geometry strongly influences the shape of the SED (e.g. Kenyon & Hartmann 1987). Strongly flaring disks, intercepting a substantial fraction of the radiation from the central star at large radii, show a rising SED peaking at around $100 \mu\text{m}$. 'Flattened' disks, on the other hand, intercept far less of the radiation from the central star, and show a power-law-like SED decreasing with wavelength. Meeus et al. (2001) showed that the disks in HAEBE systems can be divided into two groups based on the shape of their SEDs. Meeus et al. (2001) interpret this bi-modal behaviour of the SED in terms of a bi-modal disk geometry, having either a flaring or a 'flattened' disk structure. Recent spatially resolved observations seem to confirm the interpretation that the different SEDs can be linked to different disk geometries (e.g. Leinert et al. 2004). As an explanation for the different disk geometries two different models have been proposed: (1) grain growth and gravitational settling towards the disk mid-plane, and (2) 'self shadowing' of the disk surface at larger radii by the inner (~ 0.1 AU) disk.

Coagulation models show that if the dust grains in the upper layers of a flared disk become sufficiently large, they will gravitationally settle towards the mid-plane of the disk, resulting in a flattened disk geometry (e.g. Schr apler & Henning 2004; Nomura & Nakagawa 2006). Recent model calculations concerning the effect of grain coagulation and settling on the

SED show that the changing dust geometry from a flaring towards a flattened geometry due to the grain settling results in SEDs consistent with observations (D’Alessio et al. 2006; Dullemond & Dominik 2004b; Furlan et al. 2005, 2006)

As an alternative, Dullemond & Dominik (2004a) explain the variation in observed SED shapes for HAEBE and TTS systems as differences in disk heating caused by differences in the self-shadowing of the disk surface. If the central star can not directly irradiate the outer disk surface due to a puffed-up inner disk (causing the surface of the outer disk to lay in the shadow of the inner disk), the temperature and thus the scale height of the shadowed region will be substantially lower compared to a disk with a directly irradiated surface. This lower temperature will result in a smaller pressure scale height of the disk and thus in a ‘flattened’ geometry.

A way to test these models is to look for a relation between the measured grain sizes and the geometry of the disk. In Fig. 6 we explore the relation between the amorphous silicate grain sizes, as measured by the strength of the 10 μm silicate feature, and the disk flaring angle, as measured by the 30 μm over 13 μm (upper panel) and the 70 μm over 13 μm (lower panel) flux ratios. Here, the 13 μm and 30 μm fluxes are synthetic photometry points derived from our IRS spectra using an 1 μm , respectively, 2 μm wide box centered on the quoted wavelengths. The 70 μm fluxes are derived from MIPS observations. Fig. 6 provides quantitative evidence that these variables are indeed correlated. The Kendall’s τ for the top panel is 0.7 with $P = 0.03$, while for the bottom

panel $\tau = 0.81$ with $P = 0.01$, both indicating a significant positive correlation. As we saw in Fig. 5, the peak-to-continuum ratio of the 10 μm silicate features is strongly anti-correlated with grain size. As a result, we conclude from Fig. 6 that grain size is strongly correlated with SED slope. Larger flaring angles of the disk produce larger flux ratios because of enhanced emission from cooler grains further out in the disk that are exposed to the stellar flux by the flaring. With increasing grain size (decreasing 10 μm silicate band) the flaring angle of the disk appears to decrease (as traced by the slope of the SED towards longer wavelengths). Our results are in qualitative agreement with the model predictions of D’Alessio et al. (2006) and Dullemond & Dominik (2004b), and provide direct spectroscopic evidence for the link between the typical size of the dust grains and the disk structure. These results suggest that in TTS systems it is coagulation and grain settling towards the mid-plane which determines the disk geometry and thus the SED, rather than self-shadowing by the disk.

3.3. The crystalline silicates in protoplanetary disks

The analysis of features produced by crystalline silicates provides important information on dust processing in protoplanetary disks. Presently, no crystalline silicates have been observed in the diffuse ISM. Kemper et al. (2005) place an upper limit of 1% on the crystalline silicate mass fraction of the diffuse ISM. The much higher mass fractions observed in protoplanetary disks (e.g. Bouwman et al. 2001; van Boekel et al. 2005, $\sim 5\%$ in this study)

therefore, imply that the observed crystalline silicates had to be formed in the disks themselves, rather than being incorporated directly from the ISM into the disk (see Henning et al. 2005). This makes crystalline silicates a tracer of dust processing and evolution in protoplanetary disks. Figs. 7 and 8 show the observed crystalline silicate bands at mid- and far-IR wavelengths, respectively, for our TTS sample. As described in Section 2.2 the spectra have been normalized and, for the $10\ \mu\text{m}$ regime, corrected for the amorphous silicate contribution. These normalized spectra clearly show the emission bands characteristic of emission from the crystalline dust species forsterite, enstatite and silica. Using the opacities plotted in Figs. 3a to 3c, these three crystalline dust species, in combination with the amorphous silicates, produce an excellent fit to the Spitzer spectra as shown in Fig. 2. The overall mass fraction of crystalline silicates based on the spectral decomposition of the $10\ \mu\text{m}$ silicate band is around $\sim 5\%$ (see also Table 3). We find no conclusive evidence for other crystalline silicates. Interestingly, other crystalline dust species, like iron sulfides or oxides can be expected to exist in protoplanetary disks (e.g. Pollack et al. 1996). Looking at Figs. 2 and 8, weak features at $25.5\ \mu\text{m}$ (source number 0 and 5) and $30.5\ \mu\text{m}$ (source number 0 and 3) can be observed which are not properly reproduced by our dust model. These features, however, are 1) not conclusively seen in the other targets; 2) the bands do not coincide with known bands of materials like iron-sulfide or iron-oxide (Begemann et al. 1994; Henning et al. 1995); and 3) no clear relation between these weak bands can be observed. The possibility that these very

weak bands are an instrumental artifact in the form of some residual fringing can not be ruled out at this stage.

3.3.1. Crystallinity and grain size

As for amorphous dust grains, the shape, strength and wavelength positions of the emission bands of the crystalline dust species yield information on the typical size of the emitting dust grains. As the crystalline silicates have many narrow spectral features sensitive to shape, size and composition of the dust grains, an excellent determination of the grain properties can be made. Using the analysis method described in Section 2.2, Figs. 9 and 10 show the correlations between the measured position and strengths of the main forsterite resonances in our TTs sample. No trend in the band positions can be observed, which hardly vary from the nominal position expected for $0.1\ \mu\text{m}$ sized grains (filled triangles). This is in sharp contrast to the results for the amorphous silicate component, where grain sizes of at least $6\ \mu\text{m}$ are required to reproduce our observations. Also, the band ratios between the main forsterite resonances do not substantially vary from source to source. By comparing the strengths of neighbouring bands, which minimizes the influence of possible source to source variations in the mass over temperature distribution, a linear relation can be observed. This relation reflects differences in the crystalline mass fractions in the different sources, rather than differences in the grain size of the crystalline silicates. A Kendall's τ test for the data plotted in Fig. 10 results in $\tau = 0.81$ with $P = 0.011$ for the $11.3\ \mu\text{m}$ versus $10.1\ \mu\text{m}$ band strength, $\tau = 0.90$

with $P = 0.004$ for the $33.5 \mu\text{m}$ versus $27.8 \mu\text{m}$ band strength, and $\tau = 0.24$ with $P = 0.45$ for the $23.4 \mu\text{m}$ versus $27.8 \mu\text{m}$ band strength. The apparent lack of correlation between the $23.4 \mu\text{m}$ and $27.8 \mu\text{m}$ band strength most likely reflects the difficulty in fitting an accurate local continuum underneath the $23.4 \mu\text{m}$ band. Still, those sources showing the strongest $23.4 \mu\text{m}$ bands also show the strongest bands at $27.8 \mu\text{m}$.

From the spectral decomposition in the $10 \mu\text{m}$ wavelength region (see also Table 3), we determined the relative mass fraction of crystalline silicates contributing to the crystalline emission bands. Fig. 5 also shows the relation between the observed amorphous silicate grain size and the crystalline silicate mass fraction. A Kendall's τ test gives $\tau = -0.43$ with $P = 0.18$ suggesting reasonable probability that the crystallinity and grain size of the (bulk) amorphous dust are uncorrelated. Determining the mass fraction of crystalline silicates depends on how well one can determine the mass fraction of the amorphous dust component. Within the $10 \mu\text{m}$ spectral region, probing the warmest dust, this poses no problem as the amorphous silicates show a clear spectral signature. At the longer ($\sim 20 \mu\text{m}$) wavelengths, probing the colder dust at larger disk radii, however, amorphous silicates lack clear spectral signatures, which makes it difficult to determine the physical properties of the colder grains. However, the strengths of the emission bands over the local continuum in the $\sim 20 - 30 \mu\text{m}$ spectral region, still provide a measure of the relative crystalline mass fraction as a function of wavelength, and thus as a function of tem-

perature and hence as a function of radial distance in the disk. Fig. 11 compares the strength of the $10 \mu\text{m}$ silicate band -a measure of the typical grain size of the amorphous silicates- to the observed band strengths and positions of three of the main crystalline silicate bands. No conclusive correlation between the amorphous and crystalline bands can be observed, implying that both the observed crystalline mass fraction and size of the crystals are not correlated with the grain size of the amorphous dust, and thus grain growth and crystallization appear to be unrelated. A Kendall's τ test for the relation between the peak-over-continuum value versus the strength and position of the $27.8 \mu\text{m}$ band results in $\tau = 0.147$ with $P = 0.65$ and $\tau = -0.048$ with $P = 0.88$, respectively. For the the relation between the peak-over-continuum value versus the strength and position of the $33.5 \mu\text{m}$ band we find $\tau = 0.048$ with $P = 0.89$ and $\tau = 0.52$ with $P = 0.1$, and for the relation between the peak-over-continuum value versus the strength and position of the $23.4 \mu\text{m}$ band we find $\tau = 0.33$ with $P = 0.29$ and $\tau = 0.62$ with $P = 0.051$, respectively. Similar to Fig. 10, discussed in the previous paragraph, the possible weak correlation we observe for the $23.4 \mu\text{m}$ band is most likely due to a systematic problem in correctly determining the local continuum using a polynomial fit. As we can see in Fig. 1, the shape of the SED in the $20 \mu\text{m}$ region varies considerable. As we shown in Section 3.2, there is a correlation between the shape of the SED and the peak-over-continuum value of the $10 \mu\text{m}$ silicate band. The possible correlation with the $23.4 \mu\text{m}$ band, therefore, might simply reflect a systematic difference in the local

continuum estimate between source with a towards longer wavelengths rising SED and those for which the SED is decreasing.

At first glance the spectrum of a source like 1RXS J161410.6-230542 (lower left panel in Fig. 2) seems to exhibit a much higher crystalline mass fraction than a source like RX J1842.9-3532 (upper left panel Fig. 2). The apparently more pronounced crystalline silicate bands in the former TTS system, however, do not reflect a larger crystalline mass fraction but rather less amorphous silicate emission. As the amorphous grains grow with respect to the crystalline silicates, their relative opacities decrease and hence their contribution to the observed spectra diminishes. It is, therefore, crucial to have an accurate determination of the grain size of the (bulk) amorphous silicates. If we would have used a smaller maximum grain size in our spectral decomposition, we would have estimated that no amorphous silicates are present in the 1RXS J161410.6-230542 system, leading to a 100 % crystalline silicate mass fraction. This would, consequently, have led to a relation between the grain size of the amorphous dust and the crystallinity, as was noted by van Boekel et al. (2005). This result could be an artifact from underestimating the maximum grain size in their ground based observations, leading to a lower mass estimate of the amorphous dust component. Compared with these ground-based studies, we should note that the *Spitzer* data have the advantage to allow for a determination of the continuum outside of the spectral window accessible from the ground. This results in a better characterization of the strength of the 10 μm silicate band, and thus of the

grain size, especially in the case of very weak emission features.

3.3.2. *The crystallization process*

Apart from the comparison between the crystalline and the amorphous emission bands, the inter-comparison between the crystalline spectral features can provide crucial information. Though we are not spatially resolving the protoplanetary disks, from model calculations of the temperature distribution in the disk around a typical TTS, one can make an estimate of the size of the emitting region at a given wavelength (Kessler-Silacci et al. 2006b, e.g). Kessler-Silacci et al. (2006b) argue that the silicate feature at around 10 μm originates from the disk surface at round 1 AU from the central star. The spectral features observed at the longest wavelengths, at around 30 μm , correspond to a temperature of ~ 120 K; the temperature at which a black body would emit most of his radiation at the given wavelength. Assuming a λ^{-1} dependency for the dust opacity, and a typical stellar temperature and radius of 5500 K and 1 R_{\odot} , respectively, dust grains attain a temperature of 120 K at a radius of about 15 AU from the central star. This implies that with the IRS instrument we can probe the inner ~ 15 AU of a disk in a TTS system. The dust composition of the disks outward of ~ 15 AU can not be determined as the dust grains at these large radii are too cold to emit at wavelengths covered by the IRS spectrograph. Comparing the relative band strengths of forsterite in the 10 μm wavelength region probing the warmest dust, with the forsterite bands at longer wavelengths probing the colder dust com-

ponent further out in the protoplanetary disks, a possible trend can be observed (see Fig. 12). A Kendall's τ test for the relation between the 11.3 μm peak strength and the peak strengths of the 23.4, 27.8 and 33.5 μm bands results in $\tau = 0.52$ with $P = 0.1$, $\tau = 0.71$ with $P = 0.024$ and $\tau = 0.62$ with $P = 0.051$, respectively.

On average, those systems showing the strongest forsterite emission bands in the 10 μm spectral region also show the strongest bands at the longer wavelengths. One could interpret this possible correlation as evidence of a global crystallization process, where the crystallinity of the inner ~ 15 AU of the disk is increased from non-detectable ISM values to the observed mass fractions of about $\sim 5\%$ as measured in the 10 μm spectral region. Whether this means that the crystalline silicates are formed throughout the entire inner disk, or formed locally and then redistributed throughout the inner disk will be discussed in Section 4. One should note that due to the uncertainties in determining the amorphous mass fractions in a quantitative way at the longer wavelengths (see also Section 2.3), the radial density profile of the crystalline silicates remains uncertain. It is possible that in colder parts of the disk, at larger radial distances, the fraction of crystalline grains deviates from that determined for the inner parts. However, our results show that, irrespective of the exact radial profile, the crystallinity of the very inner (~ 1 AU as measured at 10 μm) and outer (~ 5 -15 AU as measured at wavelengths $\sim 20 - 30$ μm) disk regions are related.

A similar comparison for the enstatite emission bands is difficult as at the longer

wavelengths our spectra show no features which can be uniquely identified with enstatite. Comparing the strength of the main enstatite band at 9.2 μm and the longer wavelength bands of forsterite we find no clear correlation. This suggests that both crystalline species are to a certain extent unrelated, and a general increase of forsterite abundance seems not to correspond to a similar increase in enstatite abundance. Although the crystalline silicate mass relative to that of the amorphous silicates can not be determined at the longer wavelengths, our spectral decomposition as a function of wavelength, and thus radius of the emitting regions, can determine the mass ratios between the different crystalline silicates. In Fig. 13 the relation between the enstatite fraction of the crystalline grain populations as measured within the 10 μm wavelength region, and that determined from the longer wavelength spectral regions, is plotted. Surprisingly, these results imply that the mass fraction of enstatite varies in the radial direction, with a larger enstatite fraction in the warmer inner disk than in the colder outer (~ 5 to 15 AU) regions. Another difference between the forsterite and enstatite grain population is the typical grain size. The grain size of the enstatite grains (~ 1 μm) is larger than that of the forsterite grains (~ 0.1 μm). Again this points towards differences in the formation mechanism and/or conditions producing these crystalline species. The implications of the above results will be discussed in Section 4.

3.4. PAH emission in protoplanetary disks around T Tauri stars

So far, little is known about the presence of PAH molecules in disks around low-mass pre-main sequence stars. Systems with a relatively strong UV field can readily excite PAH molecules, as is observed for the more massive and luminous Herbig Ae/Be systems where clear PAH emission signatures can be seen (e.g. Meeus et al. 2001; Sloan et al. 2005). Though observations of UV poor reflection nebula and PAH laboratory measurements and models (Li & Draine 2002; Mattioda et al. 2005) show that longer wavelength photons can also excite PAH molecules, little evidence has been found for IR emission bands from stochastically heated molecules or very small grains from the circumstellar disks around low-mass stars as studied in this paper. After carefully fitting our silicate model, a residual feature centered at $8.2 \mu\text{m}$ could be seen in the model subtracted spectrum of five of the observed targets, which we tentatively identify with emission from stochastically heated PAH molecules. Fig. 14 shows the normalized residual spectrum after subtraction of the best-fit silicate model. The strongest bands can be seen in the residual spectrum of HD 143006 (#2), the most luminous source in our sample (G6/8 spectral type), which also shows clear evidence for emission bands at $6.2 \mu\text{m}$ and $11.2 \mu\text{m}$.

As the PAH molecules require stellar photons to be excited, the molecules contributing to the emission bands have to be located at the optically thin surface layers of the disk, in direct view of the central star. As many papers have shown for the Herbig Ae/Be systems (e.g. Meeus et al.

2001; Acke & van den Ancker 2004), there exists a direct correlation between the presence of PAH emission bands and the shape of the SED, a measure of the flaring angle of the disk. Those disks having an SED consistent with a flattened disk structure, and hence a less illuminated disk surface show little or now evidence of PAH emission. These results are also confirmed by spatially resolved spectroscopy showing the PAH emission bands to come from the flaring surface at larger radii of the disk (van Boekel et al. 2004b). We can observe a similar trend, where those sources having SEDs consistent with more flattened disk structures show no clear evidence for the $8.2 \mu\text{m}$ feature. This apparent correlation between the lack of the $8.2 \mu\text{m}$ feature and the flaring angle of the disk, therefore, suggests that this emission band is not due to an unidentified dust species in thermal equilibrium, but rather a stochastically heated large molecule or very small grain species at the disk surface.

Surprisingly, the observed band in the $8 \mu\text{m}$ region is not centered between 7.7 to $7.9 \mu\text{m}$, where PAH emission is usually observed. The band position at $8.2 \mu\text{m}$ has only been measured in the spectra of a few other sources. Peeters et al. (2002) observed this band position in two post-AGB stars, and Sloan et al. (2005) observed the feature in the HAEBE system HD 135344. The observed bands in these three objects, however, show a slightly broader profile than is observed in the TTS systems. The observed relatively weak or absent $6.2 \mu\text{m}$ and $11.2 \mu\text{m}$ features with respect to the $8.2 \mu\text{m}$ band is consistent with the Peeters et al. (2002) and Sloan et al. (2005) studies. Further, the HAEBE sys-

tem from the latter study showing the 8.2 μm PAH band, has the lowest UV-flux of the four systems discussed in that paper, which would be consistent with our observations of lower luminosity systems. Presently, no conclusive explanation for the carrier of the 8.2 μm feature has been put forward. We can only speculate that the chemistry, ionization state and/or structure should be substantially different for our sources compared to the PAH population in HAEBE systems. Li & Draine (2002) argue that in an environment low in UV where longer wavelength photons excite the PAHs, the PAH molecules have to be ionized and/or large to be excited. The presumably much stronger X-ray emission in the TTS systems with respect to their higher mass counterparts may play also a role here, driving a different chemistry and ionization state. On the one hand, X-ray photons may increase the electron abundance in the gas which would reduce the PAH ionization. On the other hand, a strong X-ray field could directly (multiple times) ionize the PAH molecules due to the Auger effect, and thereby change them or even destroy the smallest.

4. Discussion

The circumstellar disks in T Tauri star systems are believed to be the sites of ongoing planet formation, and thus represent an analogue for the proto-solar nebula. As the disks evolve with time, the sub-micron sized dust grains present at the formation time of the disks coagulate to form larger objects and eventually planet(esimal)s (Beckwith et al. 2000; Henning et al. 2006). By studying the characteristics and evolution of the disk

and its dust composition, valuable insights can be obtained into the processes leading to the formation of planets, and important constraints on disk and planet formation models can be derived. Also, by analogy, TTS systems can provide clues into the early evolution of the solar system. In the following we will discuss the implications of our findings presented in the previous sections. Note that our sample only spans a limited range in stellar parameters and consists of older, long surviving disks. Our conclusions are applicable to similar systems, but possible effects of stellar properties or age on the evolution of circumstellar disks can not be address directly by this study. For this our results will have to be compared to the disk properties of a larger sample, spanning a wide range in stellar properties and evolutionary stages.

4.1. Grain growth and disk structure

Based on our analysis of low-resolution infrared spectra of seven TTS systems obtained with the Spitzer Space Telescope, we find clear evidence of processing and growth of the silicate dust species present in their protoplanetary disks. We interpret observed variations in the thermal emission from amorphous silicate dust species as evidence for grain sizes which are substantially different from those observed in the ISM, and argue for grain growth within the protoplanetary disks. For the first time, we find a clear correlation between the strength of the amorphous silicate feature, measuring the typical grain size of these grains, and the shape of the mid-infrared spectral energy distribution, measuring the disk scale height, i.e., flar-

ing of the disk. In the literature, two possible explanations have been put forward to explain the differences in disk flaring: First, self-shadowing of the disk due to an enhanced scale height of the very inner parts. This prevents the central star from illuminating the surface of the outer disk, required to sufficiently heat the disk for it to flare (Dullemond & Dominik 2004a). Second, grain growth and consequent gravitational settling toward the disk mid-plane (e.g. Schr apler & Henning 2004; Nomura & Nakagawa 2006; D’Alessio et al. 2006; Dullemond & Dominik 2004b; Furlan et al. 2005, 2006). Our results, linking an increase in grain size to a decrease of the disk flaring, clearly argue for the latter explanation.

An earlier study by Apai et al. (2004), studying the brown dwarf system CFHT-BD-Tau 4, also suggested a correlation between the strength of the silicate emission band and the shape of the SED. Acke & van den Ancker (2004) studied a sample of HAEBE systems observed with the Infrared Space Observatory (ISO). Because no correlation could be found between the observed silicate emission bands and the shape of the SED, the authors concluded that their observations were consistent with the self-shadowing disk model rather than coagulation and grain settling. In apparent contradiction, Acke et al. (2004) showed a correlation between grain size, as measured by the (sub) millimeter slope of the SED, and disk flaring angle, based on the ratio of the near-to mid-IR excess. The latter results argue for coagulation and grain settling towards the mid-plane as the explanation for the observed bi-modal distribution of SEDs,

consistent with our findings here for lower mass solar-type stars.

We suspect that the correlation from IR spectroscopy of the derived grain size and the disk flaring has been missed so far for the HAEBE systems are due to the at least one order of magnitude higher stellar luminosity of A and B type stars compared to the later-type stars studied here. Observations of HAEBE systems will, therefore, probe a much larger region of the circumstellar disk than the observations of TTS or brown dwarf systems for any given wavelength, by at least a factor 2 to 3. Given that coagulation and settling are a function of density and thus radius, gradients in the observed grain size and disk structure are to be expected. Probing a much larger region of the disk, therefore, could lead to the loss of any clear correlations in the HAEBE systems.

4.2. The formation of crystalline silicates

All systems studied in this paper show emission from crystalline silicates, further evidence for dust processing within the protoplanetary disks as interstellar dust, the material present at the formation time of the disks, shows no evidence for crystalline silicates. The results of the spectral analysis of the crystalline silicate emission can be summarized as follows:

1. All observed targets show emission bands of crystalline silicates at both higher ($\sim 300 - 500$ K) temperatures, probed in the $10 \mu\text{m}$ spectral window, and lower (~ 100 K) temperatures, probed in the $30 \mu\text{m}$ spectral region.

2. The observed emission bands are consistent with emission from the pure magnesium silicates forsterite and enstatite, and silica. No conclusive evidence for other species has been found.
3. The average grain size of the crystals is much smaller than that of the amorphous silicates. While amorphous silicates requires grain sizes up to 6 μm , the crystalline emission is more consistent with a size of ~ 0.1 to 1 μm .
4. we find no conclusive evidence for a correlation between the mass fraction of the crystalline silicates and the grain size of the amorphous silicates.
5. The average grain size of the enstatite grains as derived from the modelling of the 10 μm spectral region is systematically larger than that of the forsterite grains.
6. The strength of the forsterite emission features in the 10 μm wavelength region and those at the longer wavelengths seem to be correlated. This could be interpreted as evidence that the crystalline mass fraction is increased from ISM values to the observed mass fractions of about $\sim 5\%$, throughout the entire inner ~ 15 AU of the disk.
7. We find a change in the relative abundance of the different crystalline silicates from the very inner (~ 1 AU) warm dust population, which is dominated by enstatite, compared to the

population at the colder outer disk regions at larger radii (~ 5 -15 AU), dominated by forsterite. This change in relative abundances points towards a radial dependence of either the formation mechanism of the crystalline silicates, or the (non) equilibrium conditions under which they formed, and also argues against substantial radial mixing of processed material from the inner to the outer parts of the disk (see paragraphs below for a detailed discussion).

How can we interpret the above results for the crystalline silicates in a consistent picture of the physical processes occurring in a protoplanetary disk? As all our targets show similar crystalline mass fractions and compositions, these physical processes can be expected to occur in all protoplanetary disks. The formation of forsterite and enstatite requires temperatures above ~ 1000 K (e.g. Hallenbeck et al. 2000; Fabian et al. 2000). Such high temperatures are reached near the central star where dust grains can be readily heated by the stellar radiation field. In an early active disk phase, the accretion energy can provide an additional heat source for the dust in the mid-plane regions of the inner disk (e.g. Bell et al. 2000). At these high temperatures, crystalline silicates can be formed either through annealing of the amorphous silicates (see Wooden et al. 2005, for an overview) or by gas-phase condensation/annealing and gas-solid reactions in a cooling gas (Davis & Richter 2003; Petaev & Wood 2005). Our observations show, however, that a substantial fraction of the crystalline silicates have temper-

atures (~ 100 K) far below the required crystallization temperature. This implies that either large scale radial mixing has to occur, transporting the crystalline silicates from the hot inner parts to the cooler outer disk (e.g. Bockelée-Morvan et al. 2002), or that an additional localised and/or transient heating mechanism is operating in the cooler regions of the disk, at larger radial distances from the central star. Such additional heating mechanism might be provided by shock-waves in which gas and dust grains are heated to the required temperatures of above a 1000 K (Harker & Desch 2002; Desch et al. 2005).

The question is now if our results can distinguish between different formation mechanisms and/or locations for the crystalline silicates. The presence of forsterite and enstatite, respectively the magnesium rich end members of the olivine and pyroxene solid-solution series, with no evidence for crystalline silicates containing substantial amounts of iron, suggest they formed as high-temperature, gas-phase condensates (Davis & Richter 2003; Gail 2004). The presence of high-temperature condensates at lower temperatures indicates that complete equilibrium condensation is not taking place in protoplanetary disks, else these species would have been transformed to other ferromagnesian silicates during cooling. Though the exact order in which the different dust species condense out from a cooling gas depends on the gas pressure and isolation of the condensed dust grains from the surrounding gas (Petaev & Wood 2005), most models predict forsterite to be condensed out first, followed by the formation of enstatite at slightly lower temperatures through solid-

gas reactions between forsterite and SiO_2 gas. Iron will condense out slightly before or after forsterite as metallic iron grains rather than being incorporated into silicates. The slightly larger grain size of enstatite compared to forsterite can be the result from the gas-solid reactions and the broader temperature range (and thus a longer formation window in a slowly cooling gas) under which enstatite can be formed and is stable.

An alternative formation mechanism for forsterite and enstatite is annealing of amorphous silicates without evaporating/recondensating the parent grain. The annealing process critically depends on the structure of the amorphous material and the oxygen partial pressure of the surrounding gas (i.e. reducing or oxidizing conditions). To prevent the formation of iron containing olivine and pyroxene minerals, the amorphous grains have to be annealed under reducing conditions. Davoisne et al. (2006) show that carbon combustion locking up the oxygen in the form of CO rather than in FeO, will cause the iron to precipitate as metallic particles, and not get incorporated into a silicate. Thompson et al. (2002) showed that forsterite and silica, independent of the stoichiometry of the amorphous material, will always form, but that the formation of enstatite follows through solid-solid reactions between forsterite and silica. The effectiveness and speed of this reaction critically depends on the structure of the amorphous grains. In highly porous grains, like those formed from smokes, the contact surfaces between the individual sub-units will be small and, therefore, reactions will be slow and require substantial structural

modification (like melting) of the amorphous grain. For compact glassy amorphous silicates, the formation of enstatite can proceed immediately. Similar as with direct condensation, this secondary formation of enstatite through forsterite alteration could also explain why we observe a slightly larger grain size for enstatite compared to forsterite.

Apart from the above considerations two additional observational constraints can be imposed to distinguish between annealing or condensations as the main formation mechanism for crystalline silicates, namely summary points (3) and (4). The implication of these two observations is that the simultaneous presence of both large amorphous grains and small crystalline grains is *not* caused by a preferential transformation of small amorphous grains into crystalline silicates, leaving the larger amorphous grains. Or with other words, the observed change in grain size towards larger grains is caused by grain growth rather than the removal of the smaller amorphous grain population through crystallization in a distribution of grain sizes. If the latter would have been the case, a correlation between amorphous grain size and crystalline mass fraction would have been observed. This together with the fact that no large crystalline grains are observed implies that either the crystals form as gas-phase condensates, the large amorphous aggregates are disrupted before annealing, or that the main crystallization process occurred before coagulation.

Gas-phase condensation can naturally explain any difference in grain size between the amorphous and crystalline grains. In

case of an evaporation/condensation zone in the disk, where first the amorphous grains are evaporated after which crystalline species can condense out if the gas cools, no relation between the original grain size distribution of the amorphous dust and that of the crystalline grains will exist. Annealing of large amorphous grains, on the other hand, will lead to the formation of large crystals. It is, therefore, necessary to disrupt the larger aggregates before they get annealed. A gradual heating of dust grains as they approach the hot inner disk is unlikely to fulfil this requirement. Annealing by shock waves could be a more plausible scenario, as it could also provide the mechanism to disrupt the larger amorphous aggregates. This formation mechanism would be similar as the formation scenario of chondrules (e.g. Desch et al. 2005).

In case of an early formation time of the crystalline silicates, that is before coagulation and during the high accretion phases, viscous dissipation can efficiently heat the disk up to several AU from the central star (e.g Bell et al. 2000). An early formation time would imply that the crystalline silicate content of protoplanetary disks would remain fixed during their further evolution. This is consistent with previous studies who reported no correlations between the processing of the silicates and systemic ages (e.g. van Boekel et al. 2005; Kessler-Silacci et al. 2006a, 2005), though any correlation might also be lost due to the large uncertainties in age determinations. On the other hand, all systems studied in this paper show crystalline silicates. Studies of on average younger samples show that a substantial fraction

of disks show no crystalline silicates (e.g. 50 % Kessler-Silacci et al. 2006a). This would argue in favour of crystallinity increasing with time. Further, recent studies of FU Orionis objects show no sign of crystalline silicates, independent of whether the silicate emission originates in disks or envelopes (Quanz et al. 2006; Green et al. 2006; Quanz et al. 2007). If the notion is correct that the FU Orionis type objects represent the early high accretion stages of TTS evolution, crystalline silicates should be present if the bulk of the crystalline silicates would form during the early evolution of the disks. Interestingly, Quanz et al. (2006) show that FU Orionis already shows signs of grain growth. If coagulation sets in this early, an alternative scenario for the formation of crystalline silicates is required.

Note that there is no difference in coagulation behaviour between crystalline and amorphous silicates. The difference in grain size between the crystalline and amorphous silicates can be interpreted in terms of the optical properties of larger composite aggregates. Suppose a population of small, predominantly amorphous dust grains coagulates into larger aggregates. These larger aggregates will obviously consist mainly of amorphous material but with few, from each other isolated crystalline grains which will therefore react with the radiation field as separate entities. The optical properties of such composite aggregates will likely resemble that of the combined properties of a larger amorphous grain with smaller crystalline particles, similar as is observed in cometary spectra and IDPs.

The two remaining summary points, (6) and most importantly (7), to be discussed here, place further constraints on the formation mechanism of the crystalline silicates and on the location in the disk where the crystalline silicates are forming. On the one hand our data suggests a general increase in the crystalline mass fraction in the inner ~ 15 AU of the disks, on the other hand we observe a gradient in the crystalline dust composition within this inner region. The changing forsterite over enstatite mass ratio points to differences in the condensation or annealing conditions. As discussed in the previous paragraphs, the formation of enstatite follows after the formation of forsterite. The absence or much lower enstatite mass fraction derived from the longer wavelength bands, probing the cooler dust at about 5-15 AU compared to the mass ratio derived from the $10 \mu\text{m}$ wavelength region, shows that much less or even none of the forsterite is converted into enstatite at larger radial distances from the central star. In the case of gas-phase condensation as the formation mechanism for the crystalline silicates, this implies non-equilibrium condensation conditions at larger disk radii, in contrast to the very inner disk regions. If forsterite forms locally at ~ 5 -15 AU in the disk it has to be isolated from the surrounding SiO gas before they react to form enstatite. This could be achieved by coagulation, or by rapid cooling of the surrounding gas, both inhibiting the gas-solid reactions leading to the formation of enstatite. Alternatively, in case forsterite is formed through annealing of ISM material, the low enstatite to forsterite ratio implies a rather porous structure of the amorphous silicates and brief heating events, like shocks, pre-

venting the formation of enstatite.

The high temperature region in the inner disk near the central star, is the natural location where crystallization must occur. Assuming that the inner disk region is the sole region where crystalline silicates are formed, the presence of crystalline silicates at low temperatures implies that efficient radial mixing of the processed dust from the inner disk to larger radii must occur. At the early, high accretion phases of the disk, the transport of angular momentum is expected to efficiently mix material from the hot inner to the cold outer parts of the disk (Bockelée-Morvan et al. 2002; Dullemond et al. 2006). Though at a first glance this scenario would be able to explain our observations, a strong argument against it is the radial dependency of the crystalline silicate composition: If the crystalline silicates originates from a single formation region before being distributed through the disk, the composition of the processed material would be constant with radius. Indeed, detailed disk models by Gail (2004), taking into account radial mixing, predicting the dust composition as a function of radius, show exactly this counter argument. While Gail (2004) predict the composition of the crystalline silicates in inner regions of the disk to be dominated by enstatite, consistent with our observations, the radial mixing model will also predict a large mass fraction of enstatite at larger radii, in contradiction with our results. The only way to save the radial mixing scenario is if during the active mixing phase, non-equilibrium conditions prevailed in the inner parts of the disk, forming only forsterite. This might be achieved by very rapid outward transportation of

the formed forsterite preventing prolonged heating of the grains or substantial gas-solid reactions which could lead to the formation of enstatite. During the passive, low accretion disk phases, the phase were we are observing our TTS sample, where radial mixing is not expected to be efficient, equilibrium conditions might be reached again, resulting in the observed large fraction of enstatite in the inner disks. At present, however, there is no theoretical foundation for this scenario.

The alternative model to the radial mixing scenario is the in-situ formation of crystalline silicates at radii of about 5-15 AU. As at these distances stellar radiation can not heat the dust to sufficiently high temperatures for crystallization to occur, an alternative heating mechanism is required. A promising model is the local heating of dust and gas by shock waves (Harker & Desch 2002; Desch et al. 2005). For typical densities and shock speeds, small dust grains should be efficiently heated to high temperatures up to disk radii of about 10 AU. A possible source for the shocks could be gravitational instabilities or planetary mass companions within the disk. Shock heating could provide sufficiently brief heating events such that equilibrium conditions or prolonged annealing will not occur, preventing the formation of enstatite at larger radii. In the very inner (~ 1 AU) disk, at higher densities, apart from heating by the central star, cooling can be expected to be longer such that equilibrium conditions could be reached. The suggested overall increase of the forsterite mass fraction in the inner ~ 15 AU of the disks, might reflect that spiral waves could affect the entire

disk region, causing shock to occur over a large range of radii or simply that the forsterite, produced at 5-15 AU from the central star, is accreted inwards to smaller radii. This shock-wave scenario could explain why some systems do not show any evidence for the presence of crystalline silicates at the longest or even all wavelengths (e.g. Kessler-Silacci et al. 2006a): these systems might not (yet) have produced disk instabilities or sufficiently large planetary sized objects to produce shock-waves.

Ideally, the spatial distribution of the different silicate species, should be directly determined by spatially resolved spectroscopy. Due to observational difficulties, this is at present limited to the much brighter HAEBE and the most nearby TTS systems. Using mid-IR interferometric observations obtained with the VLTI/MIDI instrument, van Boekel et al. (2004a) could spatially separate contribution to the IR emission coming from the inner ~ 2 AU of the disk, and that coming from larger radii, for a sample of HAEBE systems. These observations clearly showed that the crystalline silicates in the observed HAEBE systems are mainly concentrated in the inner, high temperature, parts of the disk, and have a composition consistent with a formation under (near) equilibrium conditions. However, before concluding that all crystalline silicates form in the inner parts of the disk, one has to realize that of the by van Boekel et al. (2004a) studied systems, show no or substantially weaker crystalline silicate bands at the longer (20-30 μm) wavelengths in their Spitzer and ISO spectra (Meeus et al. 2001, Bouwman et al, in

prep.). This suggest that these HAEBE systems, in contrast to the in disks in our TTS sample, did not witnessed substantial radial mixing or in-situ formation of crystalline silicates at larger radii, with only the very inner regions of the HAEBE disks containing observable quantities of crystalline silicates.

4.3. PAH molecules in disks surrounding T Tauri stars.

Though the main focus of this paper is the silicate dust processing we report the tentative detection of emission bands from polycyclic aromatic hydrocarbon molecules. Emission bands of PAH molecules are commonly found in environments with a strong UV flux like the circumstellar disks around HAEBE stars. As PAH molecules can contain a substantial fraction of the available carbon, and are spectroscopically easier detectable as carbon in larger grains, they can provide us with important clues concerning the carbon chemistry of circumstellar environments. Characterizing the PAH population is also important for understanding the observed gas temperatures in disks, as the stochastically heated molecules strongly influence the temperature through photo-electric heating. Since the gas temperature determines the pressure scale-height of the disk, the presence of PAH molecules can, therefore, have a substantial influence on the disk geometry. Five out of the seven TTS systems of our sample show a band at 8.2 μm we identify with emission from PAH molecules. This is the first time this band is observed in low-mass pre-main-sequence systems. The relative high fraction of systems in our sample

showing evidence for PAH molecules seems to be contradicting other studies such as the Core to Disks Spitzer legacy study by (Geers et al. 2006), which found no PAH emission around sources with spectral types later than G8. However, many studies are based on the analysis of the 6.2 and 11.3 μm PAH bands. As already noticed by Peeters et al. (2002), these latter two bands seem to be suppressed in the PAH population producing the 8.2 μm feature. Just based on the 6.2 and 11.3 μm features, we would only have detected PAH emission in the HD 143006 system, a G6/8-type star, which would be consistent with the conclusions by (Geers et al. 2006). Also, as the 8.2 μm feature coincides with the strong amorphous silicate band, one can only make a firm conclusion concerning its presence after carefully modelling the silicate emission bands. The fact that we observe a PAH band at 8.2 μm rather than the commonly observed band position between 7.7 to 7.9 μm suggests a fundamental difference in carbon chemistry between our sample and the more luminous HAEBE and F- and early G-type TTS systems. At this point we can only speculate that the difference in carbon chemistry could be linked to differences in X-ray fluxes or stellar wind properties of the intermediate-mass systems compared to those of low-mass pre-main-sequence stars. If so this could also influence the possibility and chemical path by which more complex pre-biotic organic molecules can be formed in protoplanetary disks.

A. HD 143006

HD 143006 is a well-studied (e.g. Garcia-Lario et al. 1990; Walker & Wolstencroft 1988; Sylvester et al. 1996; Coulson et al. 1998; Natta et al. 2004; Dent et al. 2005) classical T Tauri star of spectral type G6/8 which appears to be member of the Upper Scorpius OB association (Mamajek et al. 2004). It displays many T Tauri characteristics including infrared to millimeter excess (Odenwald 1986), optical emission lines (Stephenson 1986), and coronal activity revealed through x-rays (Sciortino et al. 1998). It is thus an “old” accretion disk system, with an age of 3-5 Myr.

B. RX J1612.6-1859A

RX J1612.6-1859A and RX J1612.6-1859B are the names assigned in the nomenclature of Martin et al. (1998) for a pair of emission line sources in the ρ Oph vicinity. The former object is an M0 star also known as 2MASS J16123916-1859284 or GSC 06209-01312 that has been studied only by optical spectroscopy (Martin et al. 1998; The 1964). The latter object, by contrast, is a well-known T Tauri star, also known as ScoPMS 52 (Walter et al. 1994) or Wa Oph 3 (Walter 1986). This K0 star was, in fact, the target of the FEPS observations and the source discussed in our companion paper (Silverstone et al. 2006) as not having any excess emission out to 8 μm (and indeed not out to 24 μm ; Carpenter et al., in preparation). For our IRS observations of this source, however, the IRS peak-up routine centered on to the mid-IR bright object RX J1612.6-1859A in the slit rather than RX J1612.6-1859B 20” away. The observations discussed herein are thus of RX J1612.6-1859A, an M0 emission line object.

FEPS gratefully acknowledges support from NASA through JPL grants 1224768, 12224634, and 1224566. We would like to thank Dan Watson and Pat Morris for helpful discussions regarding data reduction, Deborah Padget and Tim Brooke for assistance with the observing plan, and Betty Stobie for assistance with software development, as well as the rest of the FEPS team, the IRS instrument team, and colleagues at the Spitzer Science Center for their support. MRM is also supported through NASA’s Astrobiology Institute. JB and ThH acknowledge support from the EU Human Potential Network contract No. HPRN-CT-2002000308.

REFERENCES

- Acke, B. & van den Ancker, M. E. 2004, *A&A*, 426, 151
- Acke, B., van den Ancker, M. E., Dullemond, C. P., van Boekel, R., & Waters, L. B. F. M. 2004, *A&A*, 422, 621
- Apai, D., Pascucci, I., Sterzik, M. F., et al. 2004, *A&A*, 426, L53
- Beckwith, S. V. W., Henning, T., & Nakagawa, Y. 2000, *Protostars and Planets IV*, 533
- Beckwith, S. V. W., Sargent, A. I., Chini, R. S., & Guesten, R. 1990, *AJ*, 99, 924
- Begemann, B., Dorschner, J., Henning, T., Mutschke, H., & Thamm, E. 1994, *ApJ*, 423, L71
- Bell, K. R., Cassen, P. M., Wasson, J. T., & Woolum, D. S. 2000, *Protostars and Planets IV*, 897
- Bockelée-Morvan, D., Gautier, D., Hersant, F., Huré, J.-M., & Robert, F. 2002, *A&A*, 384, 1107
- Bohren, C. F. & Huffman, D. R. 1983, *Absorption and scattering of light by small particles* (New York: Wiley, 1983)
- Bouwman, J., de Koter, A., Dominik, C., et al. 2003, *A&A*, 401, 577
- Bouwman, J., Meeus, G., de Koter, A., et al. 2001, *A&A*, 375, 950
- Carpenter, J. M., Mamajek, E. E., Hillenbrand, L. A., & Meyer, M. R. 2006, *ApJ*, 651, L49
- Chiang, E. & Goldreich, P. 1997, *ApJ*, 490, 368
- Coulson, I. M., Walther, D. M., & Dent, W. R. F. 1998, *MNRAS*, 296, 934
- D’Alessio, P., Calvet, N., Hartmann, L., Franco-Hernández, R., & Servín, H. 2006, *ApJ*, 638, 314
- Davis, A. M. & Richter, F. M. 2003, *Treatise on Geochemistry*, Volume 1. Editor: Andrew M. Davis. Executive Editors: Heinrich D. Holland and Karl K. Turekian, Elsevier., 1, 407
- Davoisne, C., Djouadi, Z., Leroux, H., et al. 2006, *A&A*, 448, L1
- Dent, W. R. F., Greaves, J. S., & Coulson, I. M. 2005, *MNRAS*, 359, 663
- Desch, S. J., Ciesla, F. J., Hood, L. L., & Nakamoto, T. 2005, in *ASP Conf. Ser. 341: Chondrites and the Protoplanetary Disk*, ed. A. N. Krot, E. R. D. Scott, & B. Reipurth, 849
- Dorschner, J., Begemann, B., Henning, T., Jäger, C., & Mutschke, H. 1995, *A&A*, 300, 503
- Dullemond, C. P., Apai, D., & Walch, S. 2006, *ApJ*, 640, L67
- Dullemond, C. P. & Dominik, C. 2004a, *A&A*, 417, 159
- . 2004b, *A&A*, 421, 1075
- Dullemond, C. P., Dominik, C., & Natta, A. 2001, *ApJ*, 560, 957
- Dutrey, A., Guilloteau, S., Duvert, G., et al. 1996, *A&A*, 309, 493
- Fabian, D., Henning, T., Jäger, C., et al. 2001, *A&A*, 378, 228

- Fabian, D., Jäger, C., Henning, T., Dorschner, J., & Mutschke, H. 2000, *A&A*, 364, 282
- Furlan, E., Calvet, N., D'Alessio, P., et al. 2005, *ApJ*, 628, L65
- Furlan, E., Hartmann, L., Calvet, N., et al. 2006, *ApJS*, 165, 568
- Gail, H.-P. 2004, *A&A*, 413, 571
- Garcia-Lario, P., Manchado, A., Suso, S. R., Pottasch, S. R., & Olling, R. 1990, *A&AS*, 82, 497
- Geers, V. C., Augereau, J.-C., Pontoppidan, K. M., et al. 2006, *A&A*, 459, 545
- Green, J. D., Hartmann, L., Calvet, N., et al. 2006, *ApJ*, 648, 1099
- Hallenbeck, S. L., Nuth, J. A., & Nelson, R. N. 2000, *ApJ*, 535, 247
- Harker, D. E. & Desch, S. J. 2002, *ApJ*, 565, L109
- Henning, T., Begemann, B., Mutschke, H., & Dorschner, J. 1995, *A&AS*, 112, 143
- Henning, T., Dullemond, C., Wolf, S., & Dominik, C. 2006, in *Planet Formation. Theory, Observation and Experiments*, Cambridge University Press, ed. H. Klahr & W. Brandner, 113–128
- Henning, T. & Mutschke, H. 1997, *A&A*, 327, 743
- Henning, T., Mutschke, H., & Jäger, C. 2005, in *IAU Symp. 231: Astrochemistry: Recent Successes and Current Challenges*, ed. D. Lis, G. Blake, & E. Herbst, Vol. 231, 119–131
- Henning, T. & Stognienko, R. 1996, *A&A*, 311, 291
- Higdon, S. J. U., Devost, D., Higdon, J. L., et al. 2004, *PASP*, 116, 975
- Houck, J. R., Roellig, T. L., van Cleve, J., et al. 2004, *ApJS*, 154, 18
- Jäger, C., Molster, F. J., Dorschner, J., et al. 1998, *A&A*, 339, 904
- Kemper, F., Vriend, W. J., & Tielens, A. G. G. M. 2005, *ApJ*, 633, 534
- Kenyon, S. J. & Hartmann, L. 1987, *ApJ*, 323, 714
- Kessler-Silacci, J., Augereau, J.-C., Dullemond, C. P., et al. 2006a, *ApJ*, 639, 275
- Kessler-Silacci, J. E., Dullemond, C. P., Augereau, J. ., et al. 2006b, *ArXiv Astrophysics e-prints*
- Kessler-Silacci, J. E., Hillenbrand, L. A., Blake, G. A., & Meyer, M. R. 2005, *ApJ*, 622, 404
- Koike, C., Chihara, H., Tsuchiyama, A., et al. 2003, *A&A*, 399, 1101
- Koike, C., Tsuchiyama, A., Shibai, H., et al. 2000, *A&A*, 363, 1115
- Lahuis, F. & Boogert, A. 2003, in *SFChem 2002: Chemistry as a Diagnostic of Star Formation*, proceedings of a conference held August 21-23, 2002 at University of Waterloo, Waterloo, Ontario, Canada, ed. C. L. Curry & M. Fich, 335
- Leinert, C., van Boekel, R., Waters, L. B. F. M., et al. 2004, *A&A*, 423, 537
- Li, A. & Draine, B. T. 2002, *ApJ*, 572, 232

- Luhman, K. L., Joergens, V., Lada, C., et al. 2007, in *Protostars and Planets V*, ed. B. Reipurth, D. Jewitt, & K. Keil, 443–457
- Mamajek, E. E., Meyer, M. R., Hinz, P. M., et al. 2004, *ApJ*, 612, 496
- Martin, E. L., Montmerle, T., Gregorio-Hetem, J., & Casanova, S. 1998, *MNRAS*, 300, 733
- Mattioda, A. L., Hudgins, D. M., & Allamandola, L. J. 2005, *ApJ*, 629, 1188
- McCaughrean, M. J. & O’Dell, C. R. 1996, *AJ*, 111, 1977
- Meeus, G., Waters, L., Bouwman, J., et al. 2001, *A&A*, 365, 476
- Men’shchikov, A. B. & Henning, T. 1997, *A&A*, 318, 879
- Meyer, M. R., Hillenbrand, L. A., Backman, D., et al. 2006, *PASP*, 118, 1690
- Meyer, M. R., Hillenbrand, L. A., Backman, D. E., et al. 2004, *ApJS*, 154, 422
- Min, M., Dominik, C., Hovenier, J. W., de Koter, A., & Waters, L. B. F. M. 2006, *A&A*, 445, 1005
- Min, M., Hovenier, J. W., & de Koter, A. 2005, *A&A*, 432, 909
- Min, M., Waters, L. B. F. M., de Koter, A., et al. 2007, *A&A*, 462, 667
- Molster, F. J., Demyk, A., D’Hendecourt, L., & Bradley, J. P. 2003, in *Lunar and Planetary Institute Conference Abstracts*, ed. S. Mackwell & E. Stansbery, 1148–+
- Molster, F. J., Waters, L. B. F. M., & Tielens, A. G. G. M. 2002a, *A&A*, 382, 222
- Molster, F. J., Waters, L. B. F. M., Tielens, A. G. G. M., & Barlow, M. J. 2002b, *A&A*, 382, 184
- Natta, A., Testi, L., Calvet, N., et al. 2007, in *Protostars and Planets V*, ed. B. Reipurth, D. Jewitt, & K. Keil, 767–781
- Natta, A., Testi, L., Neri, R., Shepherd, D. S., & Wilner, D. J. 2004, *A&A*, 416, 179
- Nomura, H. & Nakagawa, Y. 2006, *ApJ*, 640, 1099
- Odenwald, S. F. 1986, *ApJ*, 307, 711
- Pascucci, I., Gorti, U., Hollenbach, D., et al. 2006, *ApJ*, 651, 1177
- Peeters, E., Hony, S., Van Kerckhoven, C., et al. 2002, *A&A*, 390, 1089
- Petaev, M. I. & Wood, J. A. 2005, in *ASP Conf. Ser. 341: Chondrites and the Protoplanetary Disk*, ed. A. N. Krot, E. R. D. Scott, & B. Reipurth, 373
- Pollack, J. B., Hubickyj, O., Bodenheimer, P., et al. 1996, *Icarus*, 124, 62
- Press, W. H., Teukolsky, S. A., Vetterling, W. T., & Flannery, B. P. 1992, *Numerical recipes in FORTRAN. The art of scientific computing* (Cambridge: University Press, —c1992, 2nd ed.)
- Przygodda, F., van Boekel, R., Àbrahàm, P., et al. 2003, *A&A*, 412, L43

- Quanz, S. P., Henning, T., Bouwman, J., Ratzka, T., & Leinert, C. 2006, *ApJ*, 648, 472
- Quanz, S. P., Henning, T., Bouwman, J., et al. 2007, *ApJ*, 668, 359
- Rietmeijer, F. J. M. 1988, in Lunar and Planetary Science Conference, 19th, Houston, TX, Mar. 14-18, 1988, Proceedings (A89-36486 15-91). Cambridge/Houston, TX, Cambridge University Press/Lunar and Planetary Institute, Vol. 19, 513–521
- Sargent, B., Forrest, W. J., D’Alessio, P., et al. 2006, *ApJ*, 645, 395
- Scheegerer, A., Wolf, S., Voshchinnikov, N. V., Przygodda, F., & Kessler-Silacci, J. E. 2006, *A&A*, in press
- Schräpler, R. & Henning, T. 2004, *ApJ*, 614, 960
- Sciortino, S., Damiani, F., Favata, F., & Micela, G. 1998, *A&A*, 332, 825
- Servoin, J. L. & Piriou, B. 1973, *phys. stat. sol.*, 55, 677
- Silverstone, M., Meyer, M., Mamajek, E., et al. 2006, *ApJ*, 639, 1138
- Sloan, G. C., Keller, L. D., Forrest, W. J., et al. 2005, *ApJ*, 632, 956
- Stephenson, C. B. 1986, *ApJ*, 300, 779
- Strom, K. M., Strom, S. E., Edwards, S., Cabrit, S., & Skrutskie, M. F. 1989, *AJ*, 97, 1451
- Sylvester, R. J., Skinner, C. J., Barlow, M. J., & Mannings, V. 1996, *MNRAS*, 279, 915
- Thamm, E., Steinacker, J., & Henning, T. 1994, *A&A*, 287, 493
- The, P.-S. 1964, *PASP*, 76, 293
- Thompson, S. P., Fonti, S., Verrienti, C., et al. 2002, *A&A*, 395, 705
- van Boekel, R., Min, M., Leinert, C., et al. 2004a, *Nature*, 432, 479
- van Boekel, R., Min, M., Waters, L. B. F. M., et al. 2005, *A&A*, 437, 189
- van Boekel, R., Waters, L. B. F. M., Dominik, C., et al. 2003, *A&A*, 400, L21
- . 2004b, *A&A*, 418, 177
- van Diedenhoven, B., Peeters, E., Van Kerckhoven, C., et al. 2004, *ApJ*, 611, 928
- Voshchinnikov, N. V., Il’in, V. B., Henning, T., & Dubkova, D. N. 2006, *A&A*, 445, 167
- Walker, H. J. & Wolstencroft, R. D. 1988, *PASP*, 100, 1509
- Walter, F. M. 1986, *ApJ*, 306, 573
- Walter, F. M., Vrba, F. J., Mathieu, R. D., Brown, A., & Myers, P. C. 1994, *AJ*, 107, 692
- Weidenschilling, S. J. 1997, in ASP Conf. Ser. 122: From Stardust to Planetesimals, 281
- Werner, M. W., Roellig, T. L., Low, F. J., et al. 2004, *ApJS*, 154, 1
- Wooden, D. H., Harker, D. E., & Brearley, A. J. 2005, in ASP Conf. Ser. 341: Chondrites and the Protoplanetary Disk, ed. A. N. Krot, E. R. D. Scott, & B. Reipurth, 774

This 2-column preprint was prepared with the
AAS L^AT_EX macros v5.2.

TABLE 1
ASTROPHYSICAL PARAMETERS OF PROGRAM STARS.

ID#	Name	α (2000)	δ (2000)	d [pc]	$\log(\text{Age})$ [yr]	Sp. Type	Ref. [K]	T_{eff}	A_V [mag]	L_{star} [L_{\odot}]
0	RX J1842.9-3532	18:42:57.98	-35:32:42.73	145	6.63 (4 Myr)	K2	2,3,1	4995	1.03	1.0
1	RX J1852.3-3700	18:52:17.30	-37:00:11.93	145	6.5-7 (4 Myr)	K3	2,3,1	4759	0.92	0.6
2	HD 143006	15:58:36.92	-22:57:15.35	145	6.70 (5 Myr)	G6/8	7,8,9	5884	1.63	2.5
3	RX J1612.6-1859A (2MASS J16123916-1859284)	16:12:39.18	-18:59:28.0	145	6.70 (3 Myr)	M0	11	3800	1.80	0.5
4	1RXS J132207.2-693812 (PDS 66)	13:22:07.53	-69:38:12.18	86	7.23 (17 Myr)	K1IVe	10	5228	1.22	1.3
5	RX J1111.7-7620	11:11:46.32	-76:20:09.21	163	6.69 (5 Myr)	K1	5,3,4	4621	1.30	1.6
6	1RXS J161410.6-230542 ([PZ99] J161411.0-230536)	16:14:11.08	-23:05:36.26	145	6.70 (5 Myr)	K0	7,8,6	4963	1.48	3.2

References for distance, age, spectral type – (1) Neuhauser et al. 2000; (2) Neuhauser & Forbrich 2007; (3) Hillenbrand et al. 2007, in preparation; (4) Alcalá et al. 1995; (5) Luhman 2007; (6) Preibisch et al. 1998; (7) de Zeeuw et al. 1999; (8) Preibisch et al. 2002; (9) Houck & Smith-Moore 1988; (10) Mamajek et al. 2002; (11) Martin et al. 1998.

Notes for temperature, extinction, luminosity – Spectral types are from optical spectroscopy as cited above. B-V and V-K colors are used in conjunction with spectral types to estimate effective temperatures and visual extinction values; see Carpenter et al. 2007, in preparation, for details. In the case of RX J1612.6-1859A J-H and H-K colors are used and luminosity is computed from J-band bolometric correction.

TABLE 2

OVERVIEW OF DUST SPECIES USED. FOR EACH COMPONENT WE SPECIFY ITS LATTICE STRUCTURE, CHEMICAL COMPOSITION, SHAPE AND REFERENCE TO THE LABORATORY MEASUREMENTS OF THE OPTICAL CONSTANTS. FOR THE HOMOGENEOUS SPHERES WE USED MIE THEORY TO CALCULATE THE OPACITIES. FOR THE INHOMOGENEOUS SPHERES, WE USED THE DISTRIBUTION OF HOLLOW SPHERES (DHS; MIN ET AL. 2005), TO SIMULATE GRAIN DEVIATING FROM PERFECT SYMMETRY.

#	Species	state	Chemical formula	Shape	Ref
1	Amorphous silicate (Olivine stoichiometry)	A	MgFeSiO ₄	Homogeneous	(1)
2	Amorphous silicate (Pyroxene stoichiometry)	A	MgFeSi ₂ O ₆	Homogeneous	(1)
3	Forsterite	C	Mg ₂ SiO ₄	Inhomogeneous	(2)
4	Clino Enstatite	C	MgSiO ₃	Inhomogeneous	(3)
5	Silica	A	SiO ₂	Inhomogeneous	(4)

References. — (1)Dorschner et al. (1995); (2)Servoin & Piriou (1973); (3)Jäger et al. (1998); (4)Henning & Mutschke (1997);

TABLE 3

THE BEST FIT VALUES OF THE PARAMETERS IN OUR COMPOSITIONAL FITS TO THE 8 TO 13 μm SPECTRAL REGION. THE ABUNDANCES OF THE VARIOUS DUST SPECIES ARE GIVEN AS A PERCENTAGE OF THE TOTAL DUST MASS, *excluding* THE DUST RESPONSIBLE FOR THE CONTINUUM EMISSION. ALSO LISTED IS THE MASS AVERAGED GRAIN SIZE OF THE DIFFERENT DUST SPECIES. IF A SPECIES WAS NOT FOUND, OR UNCONSTRAINED BY THE SPECTRA, THIS IS INDICATED BY A - SYMBOL. THE PAH AND CONTINUUM FLUX CONTRIBUTIONS ARE LISTED AS PERCENTAGES OF THE TOTAL INTEGRATED FLUX OVER THE 10 μm REGION, CONTAINED IN THESE COMPONENTS. THESE ARE MEASURES FOR THE RELATIVE FLUX CONTRIBUTIONS, BUT CANNOT BE INTERPRETED AS RELATIVE DUST MASSES. THE RESULTING BEST FIT MODEL SPECTRA ARE PLOTTED IN FIG. 2 (LIGHT GREY LINES).

#	χ^2	T_c [K]	T_{dust} [K]	Cont. contr.	Amorph. Olivine mass	$\langle a \rangle$	Amorph. Pyroxene mass	$\langle a \rangle$	Forsterite mass	$\langle a \rangle$	Enstatite mass	$\langle a \rangle$	Silica mass	$\langle a \rangle$	PAH contr.
8-13μm spectral region															
0	11.1 \pm 0.5	1500.0 $^{+0.0}_{-5.6}$	324.6 $^{+6.9}_{-5.6}$	0.5214 $^{+0.0009}_{-0.0009}$	0.7902 $^{+0.0063}_{-0.0063}$	1.16 $^{+0.09}_{-0.09}$	0.1787 $^{+0.0071}_{-0.0072}$	1.12 $^{+0.09}_{-0.08}$	0.0146 $^{+0.0004}_{-0.0004}$	0.1 $^{+0.0}_{-0.0}$	0.0165 $^{+0.0016}_{-0.0015}$	1.20 $^{+0.08}_{-0.09}$	-	-	0.0066 $^{+0.0000}_{-0.0000}$
1	3.4 \pm 0.3	1500.0 $^{+0.0}_{-9.2}$	257.4 $^{+3.9}_{-5.3}$	0.6361 $^{+0.0027}_{-0.0025}$	0.9872 $^{+0.0042}_{-0.0058}$	3.08 $^{+0.07}_{-0.13}$	0.0016 $^{+0.0064}_{-0.0014}$	0.1 $^{+0.0}_{-0.0}$	0.0016 $^{+0.0011}_{-0.0009}$	0.1 $^{+0.0}_{-0.0}$	0.0091 $^{+0.0036}_{-0.0038}$	1.41 $^{+0.08}_{-0.32}$	0.0006 $^{+0.0030}_{-0.0006}$	1.5 $^{+0.0}_{-0.0}$	0.0082 $^{+0.0011}_{-0.0011}$
2	17.2 \pm 0.7	1459.0 $^{+17.1}_{-13.5}$	296.2 $^{+5.3}_{-2.6}$	0.6255 $^{+0.0011}_{-0.0013}$	0.4225 $^{+0.0120}_{-0.0053}$	0.13 $^{+0.47}_{-0.03}$	0.5296 $^{+0.0047}_{-0.0137}$	5.30 $^{+0.06}_{-0.05}$	0.0149 $^{+0.0003}_{-0.0003}$	0.1 $^{+0.0}_{-0.0}$	0.0330 $^{+0.0011}_{-0.0011}$	1.496 $^{+0.004}_{-0.02}$	-	-	0.0246 $^{+0.0000}_{-0.0000}$
3	8.8 \pm 0.7	1030.6 $^{+77.5}_{-94.7}$	369.9 $^{+66.4}_{-44.0}$	0.6792 $^{+0.0263}_{-0.0210}$	0.2933 $^{+0.0511}_{-0.2375}$	6.00 $^{+0.0}_{-0.009}$	0.6452 $^{+0.2366}_{-0.2529}$	4.85 $^{+0.34}_{-1.94}$	0.0141 $^{+0.0044}_{-0.0018}$	0.15 $^{+0.24}_{-0.04}$	0.0342 $^{+0.0061}_{-0.0054}$	1.13 $^{+0.13}_{-0.13}$	0.0133 $^{+0.0040}_{-0.0027}$	0.37 $^{+0.27}_{-0.22}$	0.0103 $^{+0.0003}_{-0.0002}$
4	11.1 \pm 0.5	778.8 $^{+14.6}_{-14.8}$	183.8 $^{+11.2}_{-14.8}$	0.6054 $^{+0.0011}_{-0.0011}$	0.6369 $^{+0.0367}_{-0.0412}$	5.57 $^{+0.08}_{-0.05}$	0.3279 $^{+0.0404}_{-0.0370}$	2.27 $^{+0.45}_{-0.75}$	0.0114 $^{+0.0003}_{-0.0005}$	0.1 $^{+0.0}_{-0.0}$	0.0238 $^{+0.0013}_{-0.0026}$	0.97 $^{+0.07}_{-0.07}$	-	-	0.0126 $^{+0.0000}_{-0.0000}$
5	4.0 \pm 0.4	1500.0 $^{+0.0}_{-7.2}$	236.6 $^{+6.5}_{-7.2}$	0.8544 $^{+0.0011}_{-0.0010}$	0.8236 $^{+0.0138}_{-0.0160}$	6.0 $^{+0.0}_{-0.0}$	0.1060 $^{+0.0153}_{-0.0133}$	0.1 $^{+0.0}_{-0.0}$	0.0272 $^{+0.0025}_{-0.0023}$	0.97 $^{+0.05}_{-0.06}$	0.0349 $^{+0.0023}_{-0.0022}$	1.39 $^{+0.07}_{-0.08}$	0.0083 $^{+0.0019}_{-0.0015}$	0.35 $^{+0.27}_{-0.21}$	0.0022 $^{+0.0000}_{-0.0000}$
6	6.9 \pm 0.4	617.0 $^{+13.2}_{-7.1}$	305.1 $^{+5.6}_{-5.8}$	0.8206 $^{+0.0055}_{-0.0096}$	0.5862 $^{+0.0810}_{-0.1153}$	6.0 $^{+0.0}_{-0.0}$	0.3728 $^{+0.1200}_{-0.0802}$	5.999 $^{+0.001}_{-0.016}$	0.0058 $^{+0.0005}_{-0.0005}$	0.1 $^{+0.0}_{-0.0}$	0.0249 $^{+0.0022}_{-0.0024}$	1.21 $^{+0.08}_{-0.09}$	0.0104 $^{+0.0009}_{-0.0009}$	0.1 $^{+0.0}_{-0.0}$	0.0066 $^{+0.0000}_{-0.0001}$
17-26μm spectral region															
0	28.3 \pm 1.4	46.3 $^{+3.8}_{-1.4}$	118.0 $^{+0.0}_{-2.7}$	0.0321 $^{+0.0022}_{-0.0018}$	0.9592 $^{+0.0066}_{-0.0071}$	1.5 $^{+0.0}_{-0.0}$	0.0161 $^{+0.0073}_{-0.0069}$	0.80 $^{+0.67}_{-0.67}$	0.0192 $^{+0.0009}_{-0.0005}$	0.14 $^{+0.11}_{-0.04}$	-	-	0.0055 $^{+0.0005}_{-0.0005}$	1.5 $^{+0.0}_{-0.0}$	-
1	7.0 \pm 0.7	105.3 $^{+30.1}_{-0.6}$	84.95 $^{+0.05}_{-0.0}$	0.2529 $^{+0.0186}_{-0.0289}$	0.8650 $^{+0.0136}_{-0.0119}$	1.61 $^{+0.14}_{-0.09}$	0.1141 $^{+0.0122}_{-0.0136}$	1.5 $^{+0.0}_{-0.0}$	0.0099 $^{+0.0011}_{-0.0013}$	0.72 $^{+0.21}_{-0.24}$	0.0007 $^{+0.0015}_{-0.0006}$	0.1 $^{+0.0}_{-0.0}$	0.0104 $^{+0.0007}_{-0.0007}$	1.5 $^{+0.0}_{-0.0}$	-
2	18.8 \pm 1.0	33.0 $^{+5.4}_{-3.3}$	112.7 $^{+0.3}_{-3.9}$	0.0096 $^{+0.0047}_{-0.0024}$	0.7384 $^{+0.1520}_{-0.0195}$	1.5 $^{+0.0}_{-0.0}$	0.2459 $^{+0.0201}_{-0.1474}$	5.84 $^{+0.10}_{-0.08}$	0.0100 $^{+0.0005}_{-0.0004}$	0.1 $^{+0.0}_{-0.0}$	-	-	0.0057 $^{+0.0008}_{-0.0004}$	1.5 $^{+0.0}_{-0.0}$	-
3	5.9 \pm 0.6	18.2 $^{+6.0}_{-3.2}$	197.7 $^{+7.9}_{-6.4}$	0.0013 $^{+0.0010}_{-0.0006}$	0.1214 $^{+0.0348}_{-0.0353}$	1.5 $^{+0.0}_{-0.0}$	0.8628 $^{+0.0369}_{-0.0348}$	5.67 $^{+0.04}_{-0.03}$	0.0130 $^{+0.0007}_{-0.0007}$	0.1 $^{+0.0}_{-0.0}$	-	-	0.0029 $^{+0.0008}_{-0.0008}$	0.71 $^{+0.71}_{-0.55}$	-
4	13.0 \pm 0.8	106.0 $^{+5.4}_{-7.4}$	152.6 $^{+2.6}_{-3.9}$	0.1748 $^{+0.0513}_{-0.0388}$	0.3846 $^{+0.0912}_{-0.0594}$	1.5 $^{+0.0}_{-0.0}$	0.5881 $^{+0.0614}_{-0.0967}$	4.99 $^{+0.18}_{-0.39}$	0.0226 $^{+0.0039}_{-0.0023}$	0.1 $^{+0.0}_{-0.0}$	0.0001 $^{+0.0014}_{-0.0001}$	0.1 $^{+0.0}_{-0.0}$	0.0047 $^{+0.0010}_{-0.0009}$	1.13 $^{+0.34}_{-0.68}$	-
5	5.3 \pm 0.5	177.0 $^{+3.9}_{-2.6}$	294.5 $^{+34.6}_{-31.3}$	0.7317 $^{+0.0120}_{-0.0104}$	0.0328 $^{+0.0784}_{-0.0311}$	6.0 $^{+0.0}_{-0.0}$	0.8255 $^{+0.0368}_{-0.0717}$	1.5 $^{+0.0}_{-0.0}$	0.0996 $^{+0.0090}_{-0.0071}$	1.26 $^{+0.10}_{-0.10}$	0.0206 $^{+0.0088}_{-0.0077}$	0.1 $^{+0.0}_{-0.0}$	0.0215 $^{+0.0009}_{-0.0051}$	0.15 $^{+0.68}_{-0.05}$	-
6	3.9 \pm 0.5	340.0 $^{+9.7}_{-110.6}$	155.1 $^{+71.6}_{-13.1}$	0.6692 $^{+0.0308}_{-0.1003}$	-	-	0.9643 $^{+0.0060}_{-0.0255}$	1.43 $^{+0.85}_{-0.83}$	0.0321 $^{+0.0157}_{-0.0051}$	0.52 $^{+0.23}_{-0.29}$	0.0025 $^{+0.0040}_{-0.0021}$	0.1 $^{+0.0}_{-0.0}$	0.0012 $^{+0.0106}_{-0.0011}$	0.1 $^{+0.0}_{-0.0}$	-
26.5-35.5μm spectral region															
0	15.3 \pm 2.0	25.7 $^{+4.9}_{-6.6}$	96.7 $^{+5.2}_{-2.7}$	0.0726 $^{+0.0282}_{-0.0115}$	0.0458 $^{+0.1059}_{-0.0396}$	2.95 $^{+2.75}_{-2.39}$	0.9341 $^{+0.0392}_{-0.1055}$	0.66 $^{+0.65}_{-0.45}$	0.0165 $^{+0.0012}_{-0.0009}$	0.74 $^{+0.29}_{-0.30}$	0.0036 $^{+0.0016}_{-0.0014}$	1.08 $^{+0.41}_{-0.78}$	-	-	-
1	3.1 \pm 0.6	31.2 $^{+10.8}_{-10.8}$	89.3 $^{+12.2}_{-13.5}$	0.0515 $^{+0.0006}_{-0.0350}$	0.5475 $^{+0.3822}_{-0.3181}$	3.47 $^{+2.39}_{-2.11}$	0.4425 $^{+0.0013}_{-0.3891}$	1.78 $^{+3.33}_{-1.19}$	0.0054 $^{+0.0003}_{-0.0012}$	0.82 $^{+0.63}_{-0.63}$	0.0011 $^{+0.0014}_{-0.0009}$	0.48 $^{+1.01}_{-0.38}$	0.0035 $^{+0.0331}_{-0.0035}$	0.89 $^{+0.63}_{-0.83}$	-
2	6.0 \pm 1.0	33.6 $^{+16.2}_{-10.0}$	134.0 $^{+21.5}_{-6.8}$	0.1070 $^{+0.1931}_{-0.0649}$	0.2973 $^{+0.1866}_{-0.2574}$	5.16 $^{+0.81}_{-3.46}$	0.6921 $^{+0.2567}_{-0.1864}$	0.47 $^{+1.79}_{-0.35}$	0.0101 $^{+0.0017}_{-0.0009}$	0.47 $^{+0.42}_{-0.31}$	0.0003 $^{+0.0012}_{-0.0003}$	0.1 $^{+0.0}_{-0.0}$	0.0002 $^{+0.0045}_{-0.0002}$	0.1 $^{+0.0}_{-0.0}$	-
3	5.2 \pm 0.8	26.9 $^{+14.2}_{-16.9}$	173.8 $^{+34.9}_{-37.5}$	0.0980 $^{+0.8152}_{-0.0921}$	0.1832 $^{+0.2251}_{-0.1675}$	4.90 $^{+1.07}_{-4.52}$	0.7364 $^{+0.0955}_{-0.3726}$	1.10 $^{+0.96}_{-0.97}$	0.0708 $^{+0.0044}_{-0.0529}$	0.55 $^{+0.42}_{-0.37}$	0.0061 $^{+0.0078}_{-0.0061}$	0.1 $^{+0.0}_{-0.0}$	-	-	-
4	6.8 \pm 0.9	21.0 $^{+6.2}_{-5.3}$	104.4 $^{+1.9}_{-4.5}$	0.0259 $^{+0.0163}_{-0.0108}$	0.0866 $^{+0.0621}_{-0.0577}$	4.37 $^{+1.45}_{-2.80}$	0.8956 $^{+0.0581}_{-0.0619}$	0.28 $^{+0.51}_{-0.18}$	0.0154 $^{+0.0010}_{-0.0008}$	0.32 $^{+0.21}_{-0.17}$	-	-	0.0024 $^{+0.0089}_{-0.0023}$	0.1 $^{+0.0}_{-0.0}$	-
5	3.2 \pm 0.6	33.2 $^{+39.1}_{-16.6}$	186.2 $^{+142.1}_{-33.5}$	0.1327 $^{+0.3108}_{-0.1136}$	0.0230 $^{+0.1883}_{-0.0213}$	2.27 $^{+3.91}_{-1.28}$	0.9521 $^{+0.0218}_{-0.1950}$	0.29 $^{+1.61}_{-1.95}$	0.0165 $^{+0.0043}_{-0.0023}$	0.38 $^{+0.37}_{-0.25}$	0.0079 $^{+0.0049}_{-0.0032}$	0.82 $^{+0.60}_{-0.61}$	0.0005 $^{+0.0053}_{-0.0005}$	0.1 $^{+0.0}_{-0.0}$	-
6	4.2 \pm 0.6	15.85 $^{+59.8}_{-5.5}$	174.5 $^{+121.1}_{-19.7}$	0.0266 $^{+0.3374}_{-0.0193}$	0.0448 $^{+0.1745}_{-0.0443}$	5.67 $^{+0.34}_{-5.89}$	0.9216 $^{+0.0524}_{-0.1567}$	1.09 $^{+0.60}_{-0.89}$	0.0193 $^{+0.0060}_{-0.0022}$	0.76 $^{+0.28}_{-0.32}$	-	-	0.0137 $^{+0.1975}_{-0.0101}$	0.1 $^{+0.0}_{-0.0}$	-

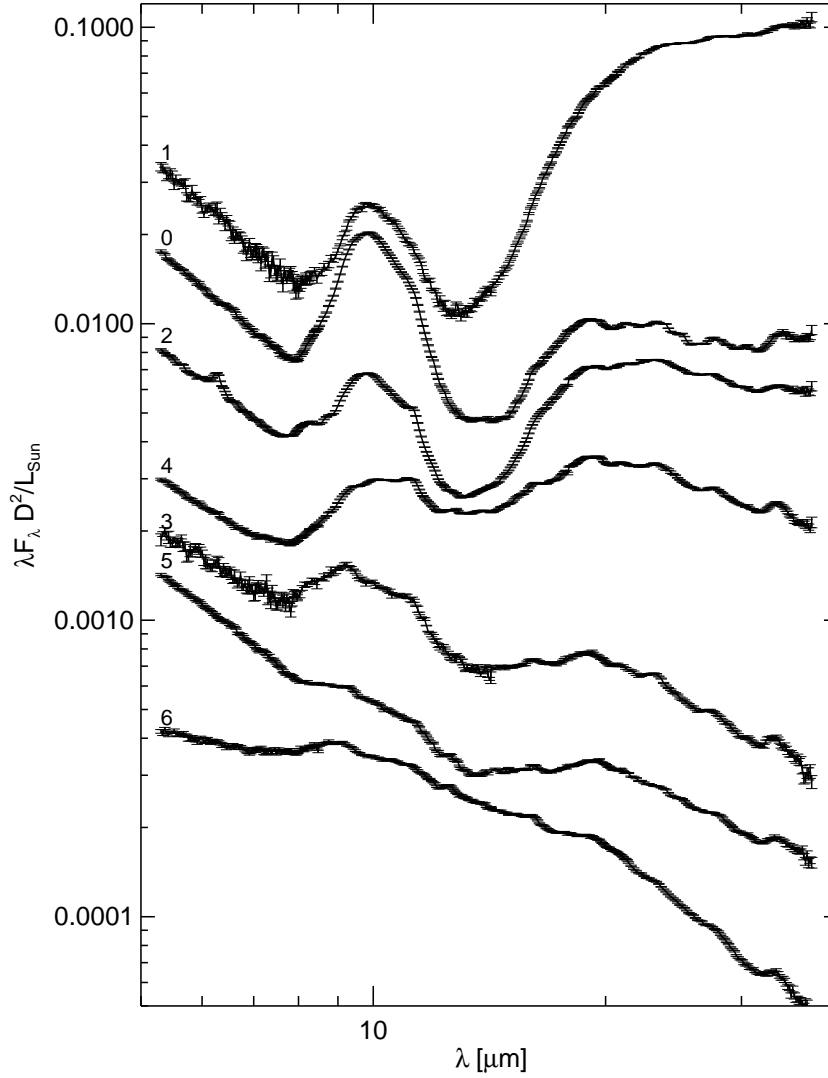


Fig. 1.— The spectral energy distributions the the TTS systems observed within the FEPS legacy program. Shown are the Spitzer low-resolution spectra scaled to the adopted distance and luminosity of the individual stars as listed in Table 1. For clarity the spectra are off-set from each other, ordered from top to bottom based on the observed slope of the SED, by multiplying by 20, 5, 0.75, 1, 2.2, 0.25 and 0.2, respectively.

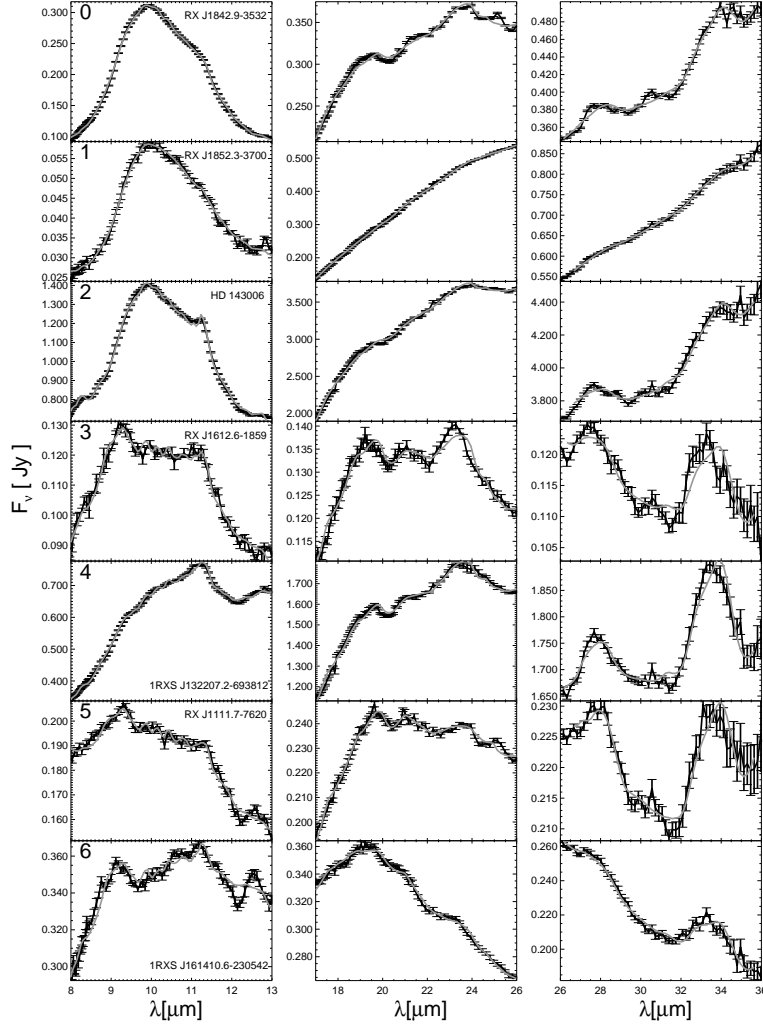


Fig. 2.— Spitzer low-resolution spectra of 7 TTS observed within the FEPS legacy program. The left panels show the spectra in the wavelength region between 8 and 13 μm . The central panels show the spectral region between 17 and 26 μm , and the right panels the spectral region between 26 and 36 μm . The spectra are ordered from top to bottom according to the decreasing strength above continuum of the 10 μm silicate band. Also plotted in this figure is a compositional fit to the spectra (light grey lines). For details on the model fits see 2.3.

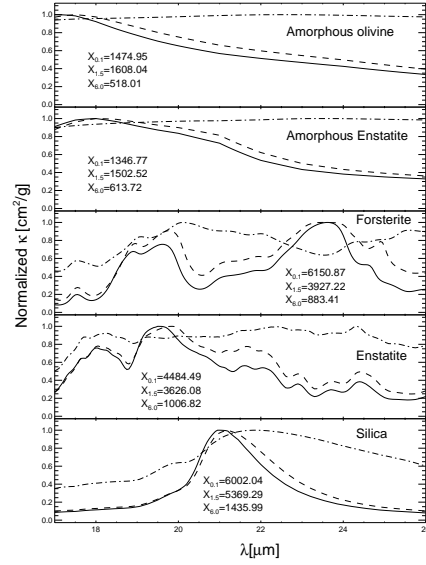
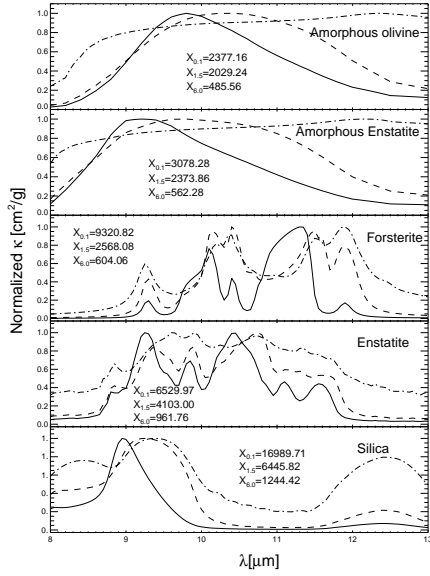


Fig. 3. — Continued.

Fig. 3.— To unity scaled opacities for the different dust species listed in Table 2. Figure 3a shows the opacities between 8 and 13 μm , Figure 3b between 17 and 26 μm , and Figure 3c between 26 and 36 μm . In each panel the solid lines represent the opacities for a grain size of 0.1 μm , the dashed lines the opacities for a 1.5 μm grain size, and the dot-dash lines the opacities of 6 μm sized grains. Also indicated in each panel are the scaling factors for each of the opacity curves, used in the normalization to unity.

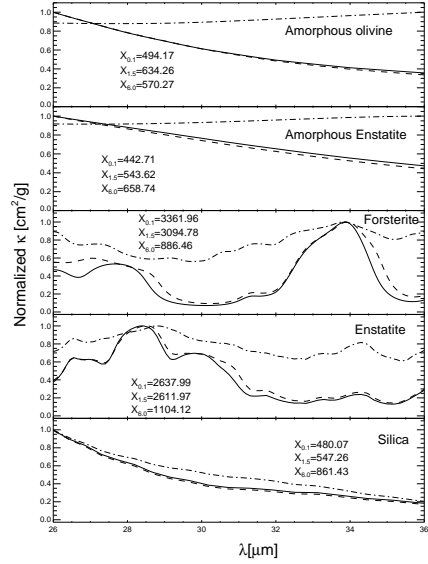


Fig. 3. — Continued.

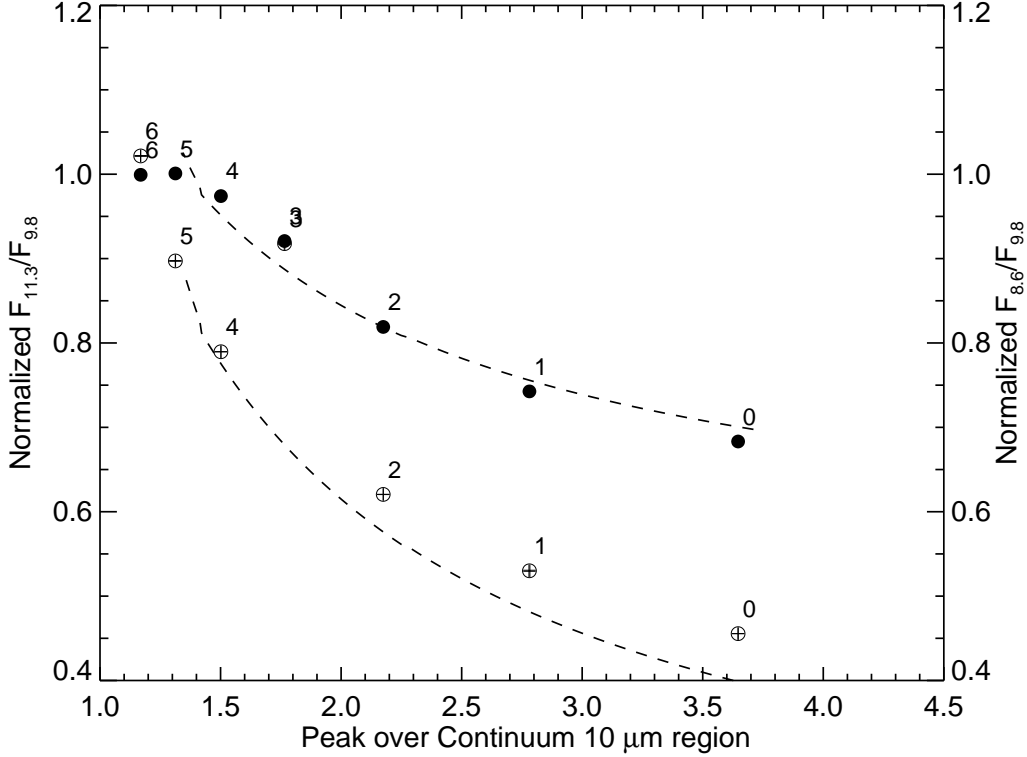


Fig. 4.— Correlations between the strength and the shape of the 10 μm silicate band. The filled symbols show the correlation between the peak over continuum ratio of the 10 μm silicate band and the ratio of the normalized flux at 11.3 μm over 9.8 μm (left axis). The open symbols show the correlation between the peak over continuum ratio and the ratio of the normalized flux at 8.6 μm over 9.8 μm (right axis). Note that the formal error on the plotted quantities is smaller than the size of the used symbols. The numbers correspond to the ID numbers of our target stars as listed in Table 1. Also plotted in this figure, represented by the dashed lines, is the calculated behavior for both flux ratios of amorphous olivine grains for a continuous changing grain size from 0.1 μm (lower right) to 2.0 μm (upper left).

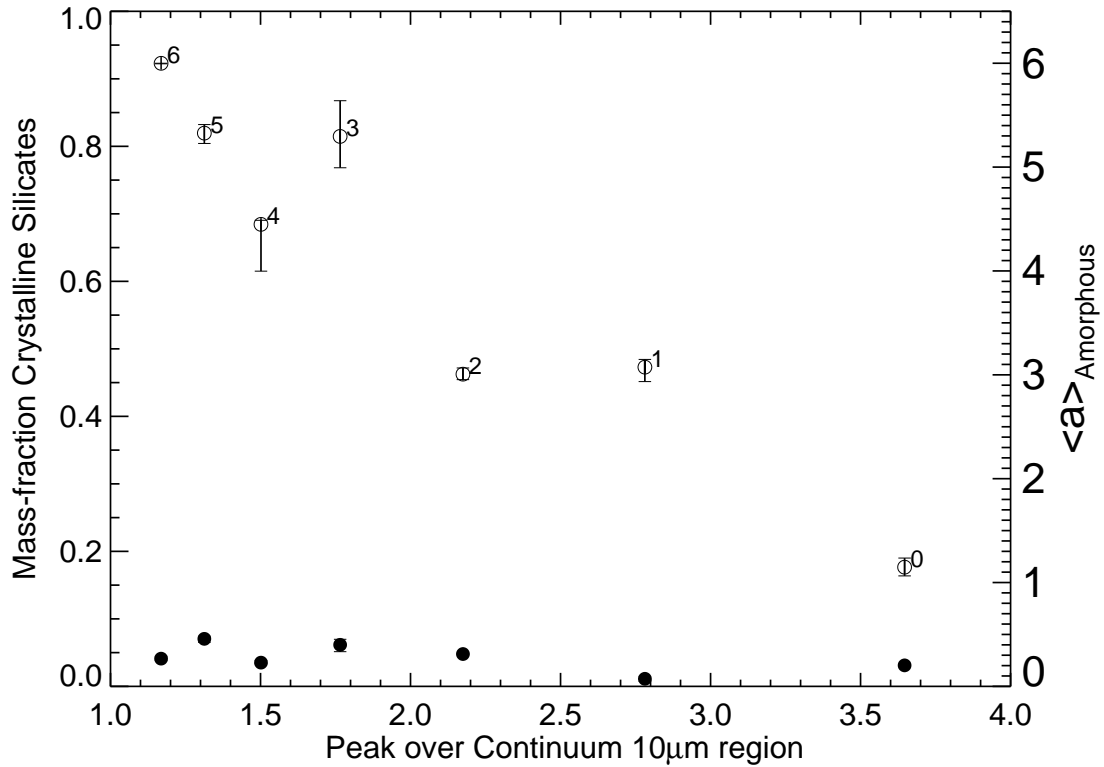


Fig. 5.— Correlation between the derived mass fraction of crystalline silicates (filled symbols; left axis) and the peak-over-continuum ratio of the $10 \mu\text{m}$ silicate band and the mass averaged grain size of the amorphous silicates (open symbols; right axis) emitting at this wavelength region. As one can see, as the amorphous grains become bigger the $10 \mu\text{m}$ silicate band becomes weaker. No correlation between the mass fraction of crystalline silicates and the typical grain size of the amorphous silicates can be observed.

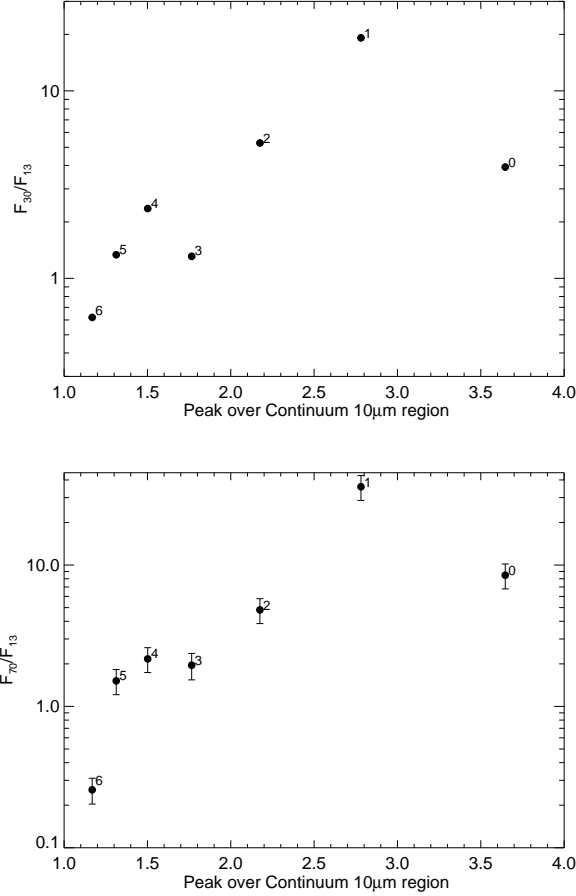


Fig. 6.— Correlation between the far-IR slope of the spectral energy distribution, a measure for disk geometry, and the peak-over-continuum ratio of the 10 μm silicate band, a measure for the typical grain size. The far-IR slope is measured by the ratio of the flux at 30 μm over 13 μm (upper panel) and the 70 μm over 13 μm flux ratio (lower panel). A clear correlation can be seen: As the 10 μm silicate band becomes weaker, the slope of the spectral energy distribution decreases. The 13 and 33 μm fluxes are synthetic photometry points derived from the *Spitzer* low-resolution spectra, the 70 μm fluxes are photometric data from the MIPS instrument on-board the *Spitzer Space Telescope*. Note that the error bars in the upper panel are the same size as the symbols and reflect the small internal uncertainties in our IRS spectra. The larger error bars in the lower panel mainly reflect the uncertainties in the absolute flux calibration between the MIPS and IRS instrument.

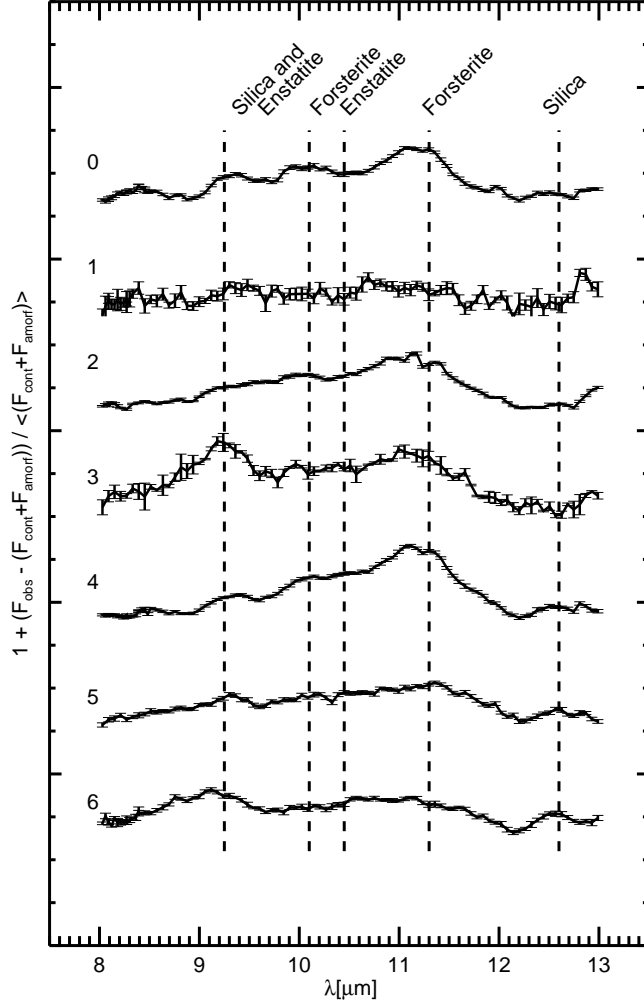


Fig. 7.— The emission bands of crystalline silicates in the 10 μm spectral window. Shown are the Spitzer low-resolution spectra normalized to the fitted amorphous silicate, PAH, and continuum model (see also Section 2.3). The normalized spectra all have the same vertical scale between 0.97 and 1.15 but are offset for clarity. The spectra are ordered from top to bottom by decreasing 10 μm silicate band strength. The ID numbers correspond to those listed in Table 1. Also indicated in this figure are the positions of the main emission bands of silica, forsterite, enstatite dust grains.

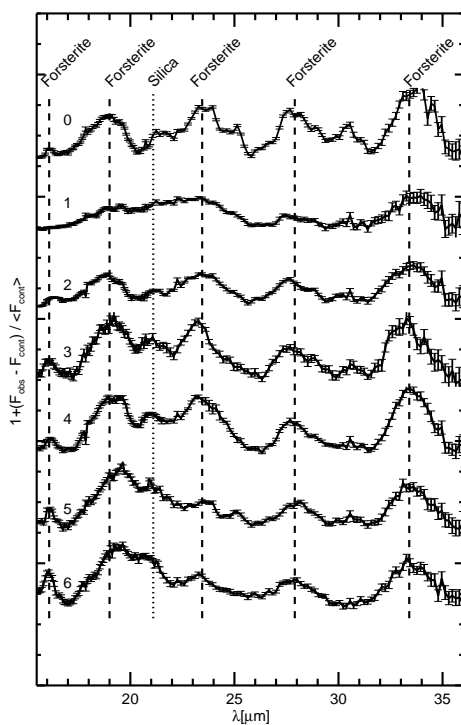


Fig. 8.— Continuum normalized spectra of the FEPS TTS sample. Shown are the Spitzer low-resolution spectra between 17 and 36 μm normalized to the fitted continuum using a low order polynomial (see also Section 2.3). The normalized spectra all have the same vertical scale between 0.97 and 1.15 but are offset for clarity. The spectra are ordered from top to bottom by decreasing 10 μm silicate band strength. The ID numbers correspond to those listed in Table 1. Also indicated in this figure with the dashed and dotted lines are the positions of the main spectral features of forsterite and silica.

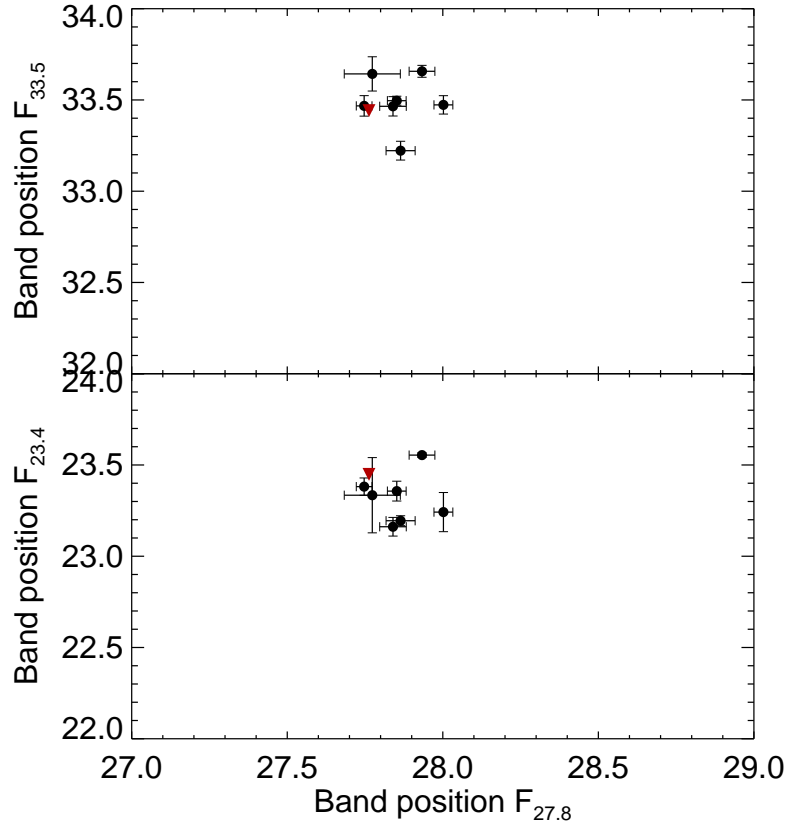


Fig. 9.— Comparison between the forsterite band position at 27.8 μm and that of the 33.5 μm feature (top panel) and the 23.4 μm feature (lower panel). Also indicated are the calculated nominal band positions for 0.1 μm forsterite grains (filled triangles).

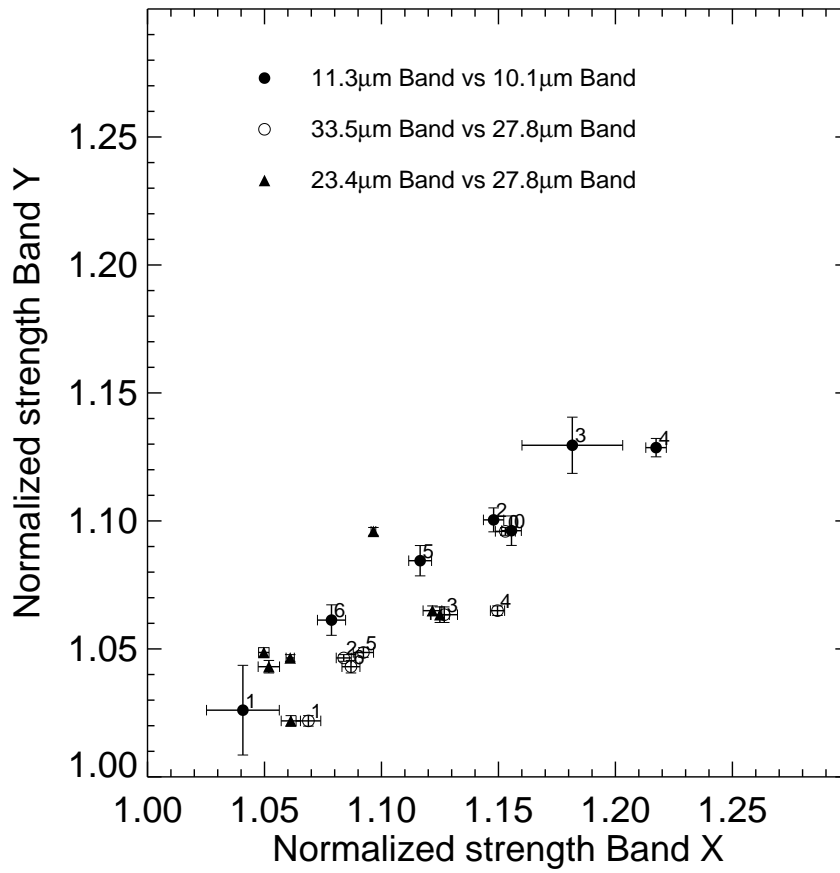


Fig. 10.— Comparison between the measured strength of the forsterite bands at 11.3 μm (plotted on x-axis) and 10.1 μm (filled circles), between the 33.5 μm (plotted on x-axis) and the 27.8 μm spectral features (open circles) and the 23.4 μm (plotted on x-axis) and the 27.8 μm spectral features (filled triangles).

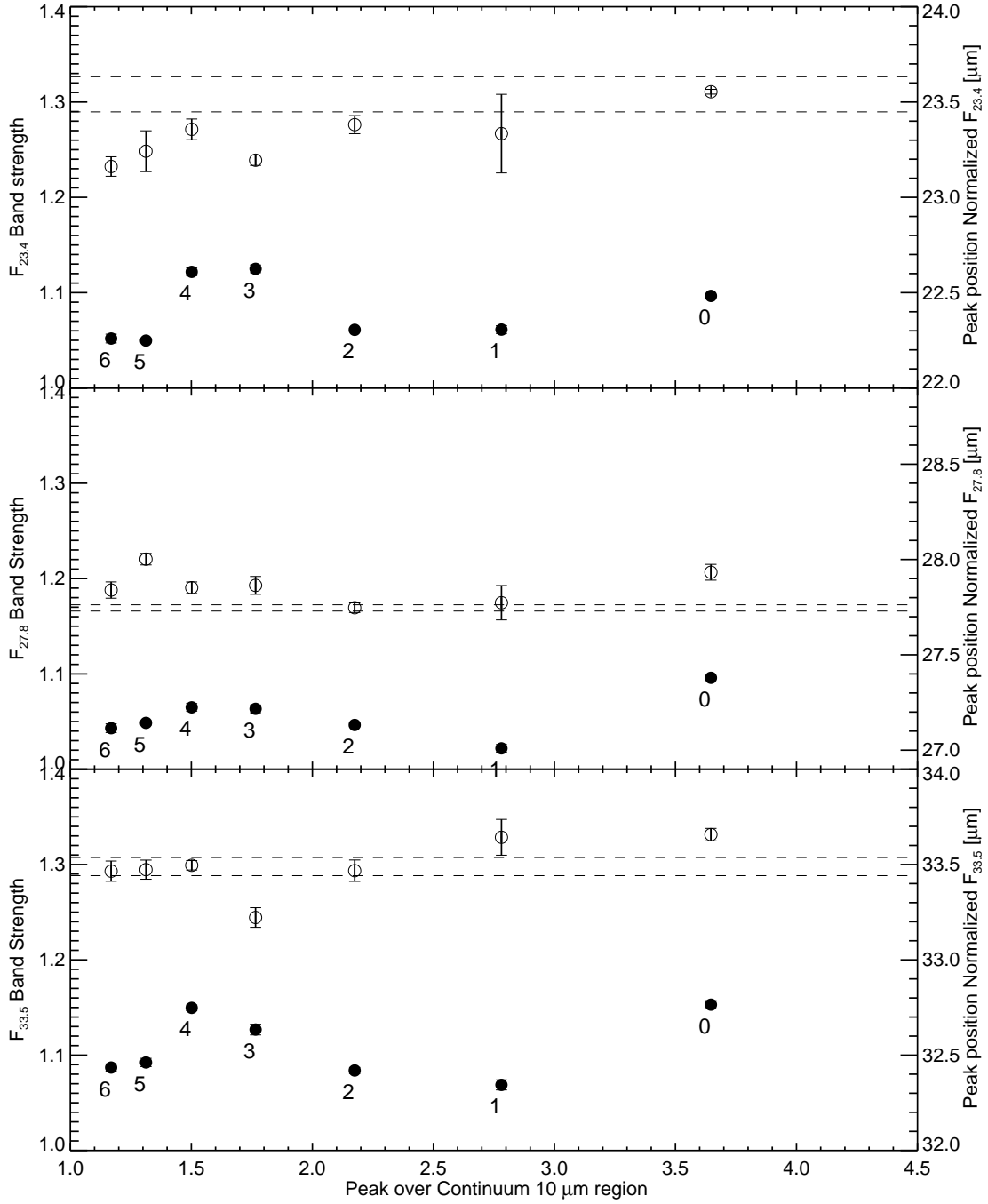


Fig. 11.— Correlations between the peak over continuum ratio of the 10 μm silicate band and the band strengths (filled symbols; left axis) and positions (open symbols; right axis) of three spectral emission bands of crystalline silicates. The top, middle and bottom panels show the correlations for the 23.4 μm , 27.8 μm , and the 33.5 μm band, respectively. As one can see, both position and normalized band strength of these crystalline silicate bands show almost no variations and are not correlated to the silicate emission at 10 μm .

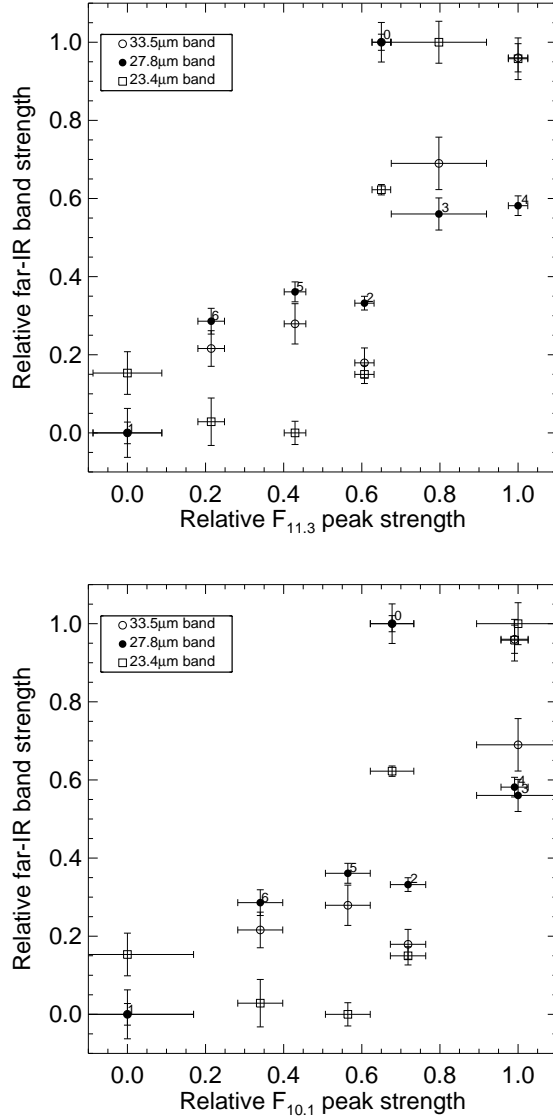


Fig. 12.— Correlations between the measured band strengths of the crystalline silicate features in the 20 to 35 μm wavelength region and those observed in the 10 μm spectral region. The top figure shows the comparison between the band strength of the 11.3 μm and that of the 33.5 μm spectral feature (open circles), the 27.8 μm band (filled circles) and 23.4 μm band (open squares), respectively. The lower figure shows a similar comparison but with the band strength of the 10.1 μm spectral feature.

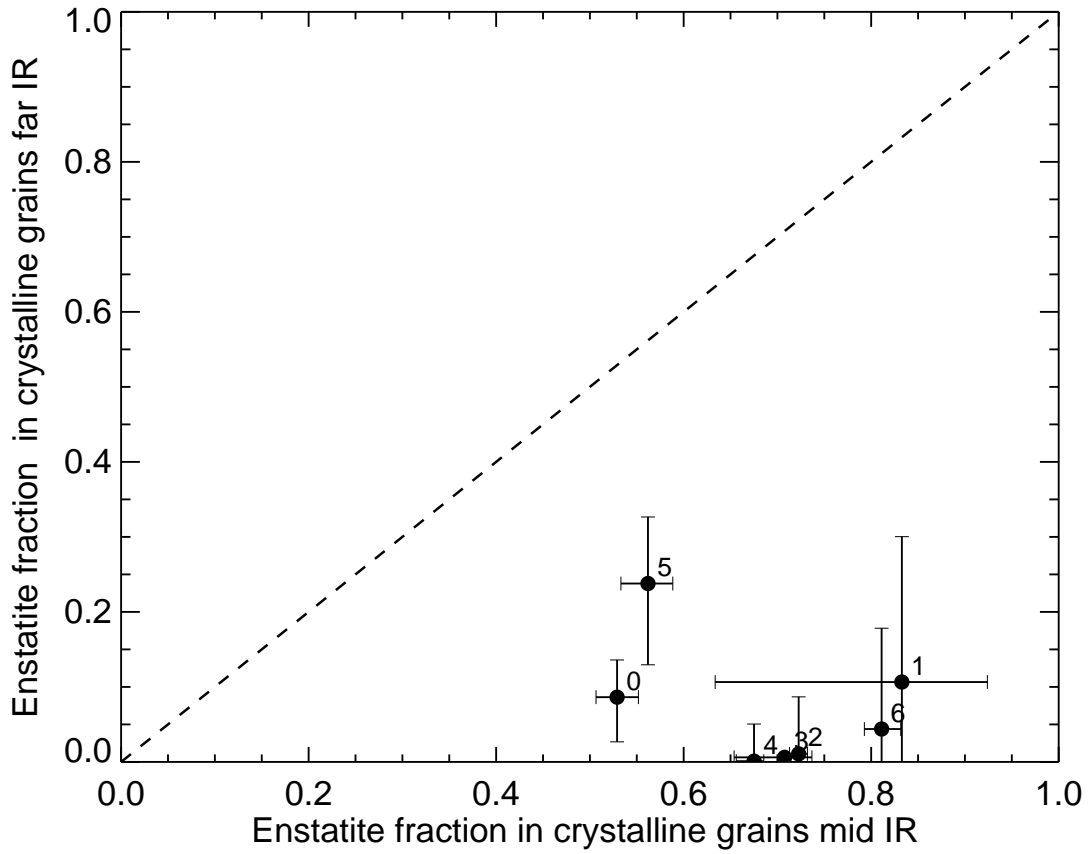


Fig. 13.— Correlation between the enstatite mass fraction of the crystalline silicates as measured in the $10\ \mu\text{m}$ spectral window and the enstatite mass fraction of the crystalline silicates derived from analyzing the longer wavelength features between 20 to $35\ \mu\text{m}$.

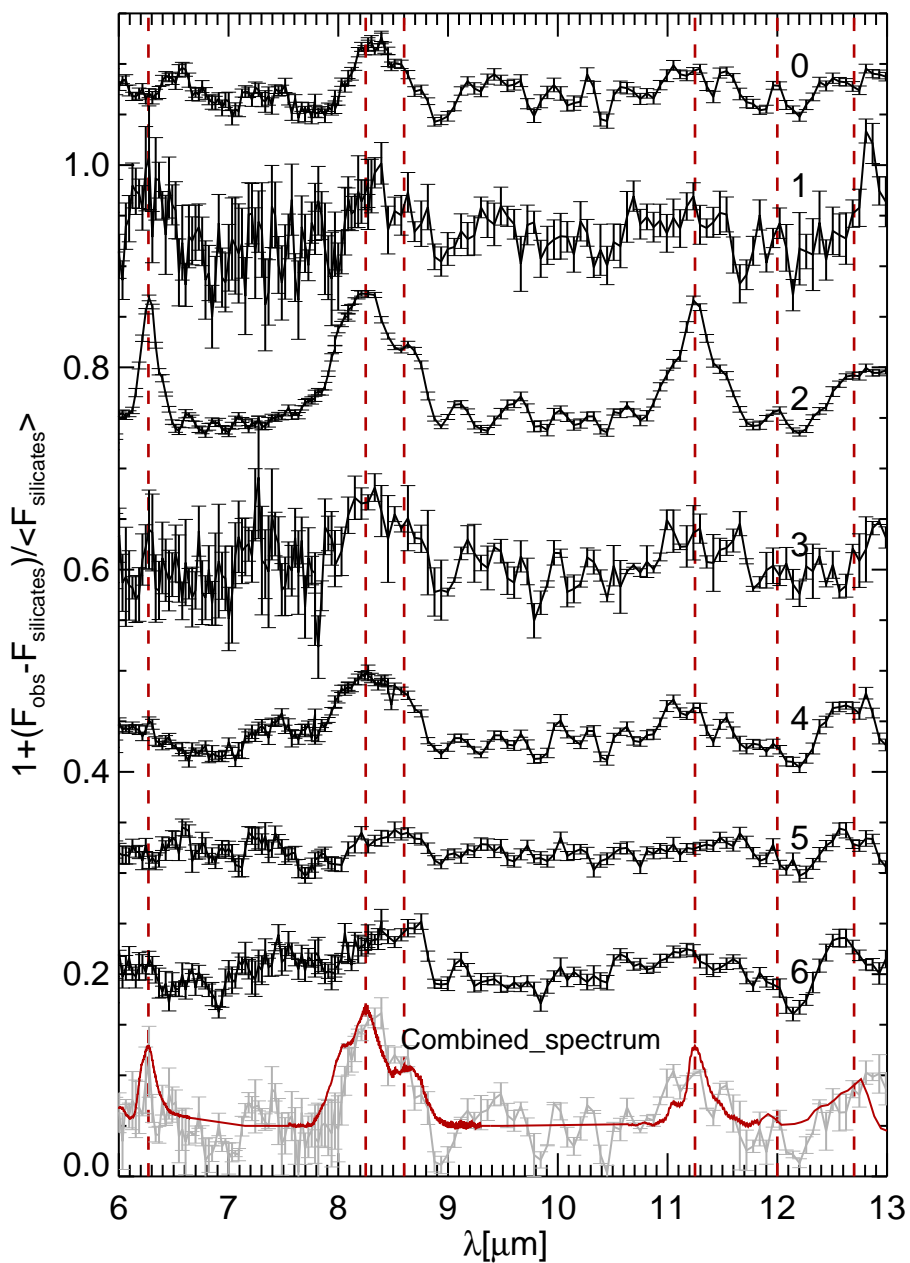


Fig. 14.— Observed PAH emission bands in the spectra of the FEPS TTS sample. Shown are the Spitzer low-resolution spectra normalized to the fitted silicate model (see also Section 2.2 and Table 3). The first 5 spectra clearly show an emission feature at $8.2 \mu\text{m}$ we assign to emission from PAH molecules. Shown at the bottom of the figure is the average spectrum of source # 0,1,3 and 4, over-plotted with the PAH template spectrum used in our fitting procedure. The dashed lines mark the positions of the main PAH bands.